








## The polymict carbonaceous breccia Aguas Zarcas: A potential analog to samples being returned by the OSIRIS-REx and Hayabusa2 missions

Imene KERRAOUCH <sup>1,2,3\*</sup>, Addi BISCHOFF <sup>1</sup>, Michael E. ZOLENSKY <sup>2</sup>, Andreas PACK<sup>4</sup>, Markus PATZEK <sup>1</sup>, Romy D. HANNA <sup>5</sup>, Marc D. FRIES <sup>2</sup>, Dennis HARRIES<sup>6</sup>, Yoko KEBUKAWA <sup>7</sup>, Loan LE<sup>8</sup>, Motoo ITO<sup>9</sup>, and Zia RAHMAN<sup>8</sup>

<sup>1</sup>Institut für Planetologie, University of Münster, Wilhelm-Klemm Str. 10, Münster D-48149, Germany

<sup>2</sup>Astromaterials Research and Exploration Science, NASA Johnson Space Center, Houston, Texas 77058, USA

<sup>3</sup>Department of Geology, University of Science and Technology Houari Boumediene (USTHB), Bab Ezzouar 16111, Algeria

<sup>4</sup>Universität Göttingen, Geowissenschaftliches Zentrum, Goldschmidtstr. 1, Göttingen D-37077, Germany

<sup>5</sup>Jackson School of Geosciences, University of Texas, Austin, Texas 78712, USA

<sup>6</sup>Institut für Geowissenschaften, Friedrich-Schiller-Universität Jena, Carl-Zeiss-Promenade 10, Jena 07745, Germany

<sup>7</sup>Faculty of Engineering, Division of Materials Science and Chemical Engineering, Yokohama National University, 79-1 Tokiwadai, Hodogaya Ward, Yokohama, Kanagawa 240-8501, Japan

<sup>8</sup>Jacobs JETS, Johnson Space Center, 2101 NASA Parkway, Houston, Texas 77058, USA

<sup>9</sup>Japan Agency for Marine-Earth Science Technology (JAMSTEC), Kochi Institute for Core Sample Research, 200 Monobe Otsu, Nankoku City, Kochi 783-8502, Japan

\*Corresponding author. E-mail: ikerraou@uni-muenster.de

(Received 22 August 2020; revision accepted 01 December 2020)

**Abstract**—On April 23, 2019, a meteorite fall occurred in Aguas Zarcas, Costa Rica. According to the Meteoritical Bulletin, Aguas Zarcas is a brecciated CM2 chondrite dominated by two lithologies. Our X-ray computed tomography (XCT) results show many different lithologies. In this paper, we describe the petrographic and mineralogical investigation of five different lithologies of the Aguas Zarcas meteorite. The bulk oxygen isotope compositions of some lithologies were also measured. The Aguas Zarcas meteorite is a breccia at all scales. From two small fragments, we have noted five main lithologies, including (1) Met-1: a metal-rich lithology; (2) Met-2: a second metal-rich lithology which is distinct from Met-1; (3) a brecciated CM lithology with clasts of different petrologic subtypes; (4) a C1/2 lithology; and (5) a C1 lithology. The Met-1 lithology is a new and unique carbonaceous chondrite which bears similarities to CR and CM chondrite groups, but is distinct from both based on oxygen isotope data. Met-2 also represents a new type of carbonaceous chondrite, but it is more similar to the CM chondrite group, albeit with a very high abundance of metal. We have noted some similarities between the Met-1 and Met-2 lithologies and will explore possible genetic relationships. We have also identified a brecciated CM lithology with two primary components: a chondrule-poor lithology and a chondrule-rich lithology showing different petrologic subtypes. The other two lithologies, C1 and C1/2, are very altered and possibly related to the CM chondrite group. In this article, we describe all the lithologies in detail and attempt a classification of each in order to understand the origin and the history of formation of the Aguas Zarcas parent body.

### INTRODUCTION

At 21:07 local time on April 23, 2019, a meteorite fall occurred in Aguas Zarcas, San Carlos County, Alajuela province, Costa Rica. The meteorite is officially named “Aguas Zarcas” in the Meteoritical Bulletin and is a

brecciated carbonaceous chondrite with total recovered mass of at least 27 kg. Based on the information in the Meteoritical Bulletin, hundreds of fusion-crust stones ranging from 0.1 to 1868 g were recovered.

According to earlier studies reported in the Meteoritical Bulletin, the interior of the brecciated

stones is uniformly dark gray and studded with small light-colored speckles. Several lithologies are mentioned in the initial classification (1) a chondrule-poor clast-type constituting of ~80 vol% of the broken surfaces of ~2 kg of material having about 10 vol% chondrules, (2) a chondrule-rich lithology with about 40 vol% chondrules, and (3) clasts with even lower chondrule to matrix ratio (one 3 g half stone shows <1 vol% of chondrules). The dominant chondrule-poor lithology shows scattered small chondrules (mean diameter of 275  $\mu\text{m}$ ,  $n = 40$ ), with prominent fine-grained rims (The Meteoritical Bulletin). The chondrule size is consistent with that of CM chondrites (Rubin and Wasson 1986). The previous oxygen and geochemical results indicate consistence with CM chondrites (Meteoritical Bulletin).

In this paper, we describe the petrography and mineralogy of the different lithologies of the Aguas Zarcas meteorite from our samples including bulk oxygen isotope data of some lithologies. We describe all the fragments in detail and attempt a classification of each lithology in order to understand the origin and the history of formation of the Aguas Zarcas parent body. This study sheds additional light on the large petrological diversity and processing of hydrous carbonaceous chondrites in the early solar system.

## SAMPLES AND ANALYTICAL TECHNIQUES

### Samples

Many stones were recovered of Aguas Zarcas, some before and some after rainfall. We therefore tried to investigate a larger number of fragments in order to determine as many of the lithologies as reasonably possible in this brecciated meteorite. The study includes several thin sections of Aguas Zarcas: PL19111, PL19112, and PL19125 prepared from the fragment MS-2 (MS = Münster), a 2.5 g pre-rain fragment stored at the Institut für Planetologie (IfP), University of Münster. Polished mounts of separate pre-rain stones provided by Robert Ward called JSC-Mount1, JSC-Mount2, and JSC-Mount3 (hereafter Mount 1, Mount 2, and Mount 3) now stored at the Astromaterials Research and Exploration Science (ARES), NASA Johnson Space Center. Additionally, JSC-40, a 40 g post-rain stone (from a dealer); JSC-6, a 6 g pre-rain stone from Robert Ward (stored at NASA JSC); and UTA-2, a 2.53 g sample from the University of Texas at Austin were included in this study, and two additional pre-rain samples CR19.19 and CR19.29 from Robert Ward. We distinguish five main lithologies, which we describe and discuss as (1) Met-1: a metal-rich lithology; (2) Met-2: a second metal-rich lithology; (3) a brecciated

CM lithology; (4) a C1/2 lithology; and (5) a C1 lithology.

Table S1 in supporting information summarizes the different fragments of Aguas Zarcas indicated above with their characteristics and lithologies.

Some sections of CM chondrites (Moapa Valley [PL20076], Banten-CM [PL93094], Maribo-CM [PL09089], and NWA12651-CM [PL17261]) and the ungrouped chondrite Acfer 094 (PL93040) have been studied here for the purpose of comparison.

### Optical and Electron Microscopy

The samples were characterized by optical microscopy and SEM/EDS at the E-Beam Laboratories of the NASA Johnson Space Center and at the Institut für Planetologie (IfP), University of Münster. We used a ZEISS polarizing microscope (Axiophot) for optical microscopy in transmitted and reflected light at the latter institute.

Chondrule diameters were measured by two different methods (1) in transmitted light (MTL) using a calibrated reticle and (2) using backscattered electron images (BSE). The maximum length and the greatest width perpendicular to the long axis of each chondrule were measured and averaged—the size is the mean of the length and width. We also measured chondrule sizes of three other CM chondrites (Maribo [PL09089], Banten [PL93094], and NWA 12651 [PL17261]) using the first method (MTL) to test the reliability of our results and to compare them with literature data of chondrule sizes in CMs.

A JEOL 6610-LV electron microscope (SEM) at the Interdisciplinary Center for Electron Microscopy and Microanalysis (ICEM) at the University of Münster was used to study the petrography and mineralogy of some samples. For quantitative analysis, samples and appropriate mineral standards were measured at an excitation voltage of 20 kV, and the beam current constancy was controlled by a Faraday cup. The attached EDS system was used for chemical characterization and analyses of the different mineral constituents (e.g., silicates, sulfides, and metals). Olivine (Mg, Fe, Si), jadeite (Na), plagioclase (Al), sanidine (K), diopside (Ca), rutile (Ti), chromium-oxide (Cr), rhodonite (Mn), Co-metal (Co), and pentlandite (Ni, S) were used as natural and synthetic standards. We used the INCA analytical program provided by Oxford Instruments for these analyses.

Some samples were imaged and analyzed at Astromaterials Research and Exploration Science (ARES) Office, NASA JSC (Houston), using a JEOL 7600-FE scanning electron microscope and JEOL 8530-FE electron microprobe. Natural mineral standards were used. Raman analyses were performed using the Ratasoskr instrument at ARES, which is a WITec

alpha-300R customized for Raman imaging at square-centimeter scales. Analyses were performed using a 488 nm excitation laser.

### Electron Microprobe Analysis (EPMA)

Most quantitative mineral analyses were obtained using a JEOL JXA 8530F electron microprobe (EPMA) at the Institut für Mineralogie (University of Münster), which was operated at 15 kV and a probe current of 15 nA. These natural and synthetic standards were used for wavelength dispersive spectrometry: jadeite (Na), kyanite (Al), sanidine (K), chromium oxide (Cr), San Carlos olivine (Mg), hypersthene (Si), diopside (Ca), rhodonite (Mn), rutile (Ti), fayalite (Fe), apatite (P), celestine (S), and NiO (Ni).

For analyses of the fine-grained materials (tochilinite–cronstedtite intergrowths (TCIs), matrix, dust rims) of the Met-1 and brecciated CM lithologies of Aguas Zarcas, the concentrations of the following elements were obtained: Na, K, S, Mg, Al, Si, P, Ca, Cr, Ti, Mn, Fe, Co, Ni. Oxygen was measured separately and calculated later for each element as an oxide in wt% for comparison. The analyses were done with variable spot sizes between 5 and 20  $\mu\text{m}$  depending on the different sizes of TCIs and rims.

Additional quantitative mineral analyses were obtained using a JEOL JXA 8530F electron microprobe (EPMA) at the ARES E-Beam Laboratory. The instrument was operated at 15 kV and a probe current of 20 nA.

### X-Ray Computed Tomography

We imaged three individual stones, UTA-2, JSC-40, and JSC-6, at the University of Texas high-resolution X-ray computed tomography (UTCT) facility on a custom-built North Star Imaging Inc. (NSI) scanner using a 225 kV FeinFocus microfocal X-ray source and Perkin Elmer 2048  $\times$  2048 flat-panel detector. The two smaller samples were scanned at 85 kV and 0.3 mA and the larger sample at 100 kV and 0.3 mA, all using an aluminum foil filter to reduce beam hardening artifacts (Hanna and Ketcham 2017). A beam hardening correction was applied to all scans using NSI software during reconstruction, and a post-reconstruction ring correction (in-house UTCT software) applied to the UTA-2 and JSC-6 sample scans. The final reconstructed voxel (3-D pixel) sizes were 9.68  $\mu\text{m}$  (UTA-2), 11.1  $\mu\text{m}$  (JSC-6), and 17.8  $\mu\text{m}$  (JSC-40).

### Focused Ion Beam (FIB)

We made one focused ion beam (FIB) section from an organic-rich matrix area of the Met-2 lithology from

JSC-mount3, and two from CM matrix in CR19-001, a pre-rain sample. The JSC-mount3 FIB was cut from a carefully selected position on the polished section at the ARES E-beam lab using a Quanta 3-D FEG DualBeam FIB instrument equipped with two XEDS detectors for chemical analysis, including spectrum collection and qualitative and quantitative elemental mapping. We cut the FIB section to approximately 100 nm thickness.

### O-Isotope Analysis

The oxygen isotopic composition of different lithologies from Aguas Zarcas was analyzed by means of laser fluorination in combination with gas source mass spectrometry (Sharp 1990). Each sample was loaded along with San Carlos olivine in a 19 pit stainless steel sample holder. The samples were fluorinated with ~50–100 mbar  $\text{BrF}_5$ . The unwanted gaseous reaction products (mainly  $\text{BrF}_{5-x}$  and  $\text{SiF}_4$ ) were removed by means of cryogenic trapping. The sample  $\text{O}_2$  was collected at  $-196^\circ\text{C}$  on a 5  $\text{\AA}$  molecular sieve for 7 min. For further purification (removal of  $\text{N}_2$  and  $\text{NF}_3$ ), sample  $\text{O}_2$  was transported with a He carrier gas stream through a 3 m long packed molecular sieve gas chromatography column (Restek) that was kept at  $50^\circ\text{C}$ . The sample  $\text{O}_2$  was then collected downstream in a second, low volume molecular sieve trap. After evacuation of He from the second trap, sample  $\text{O}_2$  was expanded to  $\sigma$  the bellows of a Thermo MAT253 gas source mass spectrometer. The sample gas was analyzed relative to a working gas for ~40 min (60 cycles). The external reproducibility of San Carlos olivine measurements was 0.1‰ for  $\delta^{18}\text{O}$  and 0.006‰ for  $\Delta^{17}\text{O}$  (1 $\sigma$  SD, single analysis). The data were normalized to the composition of San Carlos olivine ( $\delta^{17}\text{O}_{\text{VSMOW2}} = 2.715$ ,  $\delta^{18}\text{O}_{\text{VSMOW2}} = 5.220$  ‰; see Pack et al. 2016).

## RESULTS

### General Characterization of Aguas Zarcas

#### XCT Observations

The XCT data of the three samples show a diverse collection of lithologies within the Aguas Zarcas meteorite (Fig. 1 and movie files *Aguas\_Zarcas\_2.5g.mp4*, *Aguas\_Zarcas\_6g.mp4*, and *Aguas\_Zarcas\_40g.mp4* in supporting information). Because X-ray attenuation is strongly dependent on the mean atomic number  $Z$  (Hanna and Ketcham 2017), XCT data resemble backscattered electron images where different grayscales within the image represent varying chemical compositions (primarily the proportion of Fe) and the darkest voxels are pore space and fractures. Both the JSC-40 and JSC-6 samples are highly brecciated displaying several types of clasts within them (Fig. 1).

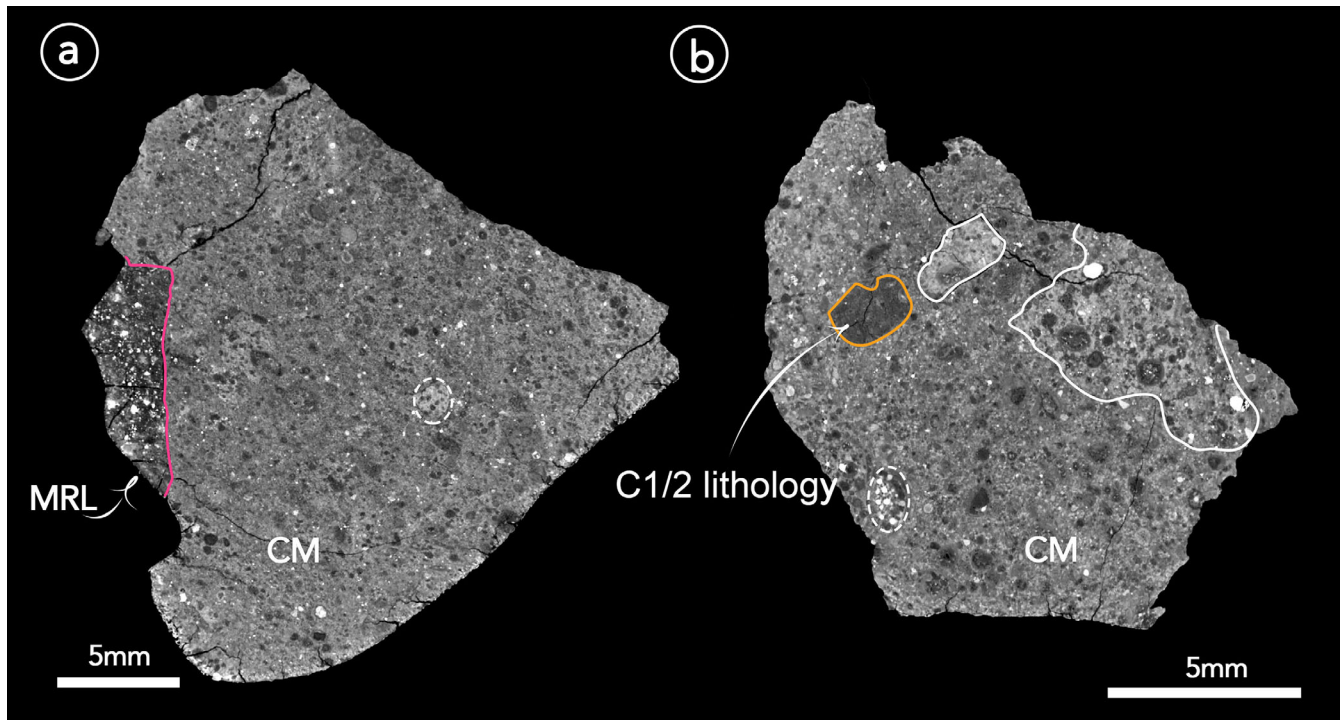


Fig. 1. a) XCT slice of JSC-40 sample showing different lithologies including a lithology that may be similar to the metal-rich lithology (MRL). b) XCT slice of 6 g sample showing fragments of several different CM subtypes including the C1/2 lithology.

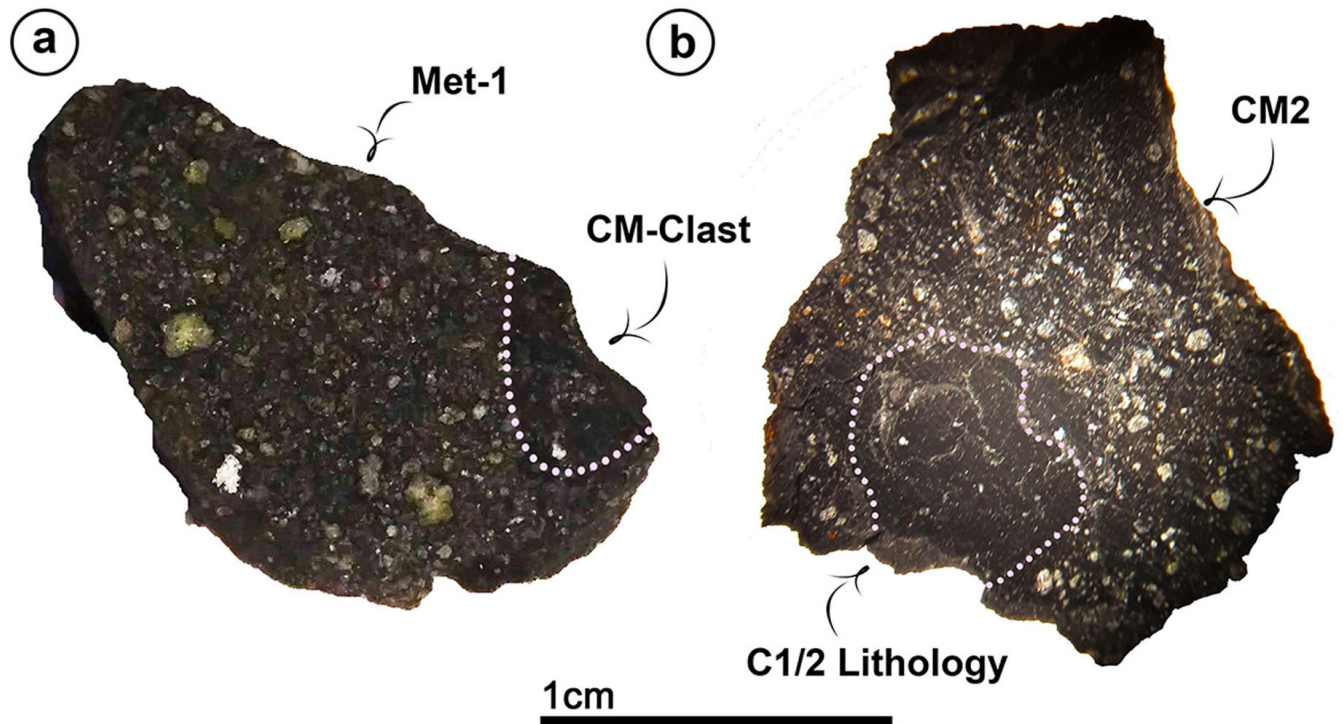


Fig. 2. a) MS-2 fragment of Aguas Zarcas chondrite studied here that consists of the Met-1 (MRL; ~80 vol%) and a small part of a brecciated CM chondrite having fragments of different subtypes of aqueous alteration; transmitted light images (PL19111 and PL19125). b) CR19.19 fragment including the C1/2 lithology within the CM part; transmitted light image (PL19149).



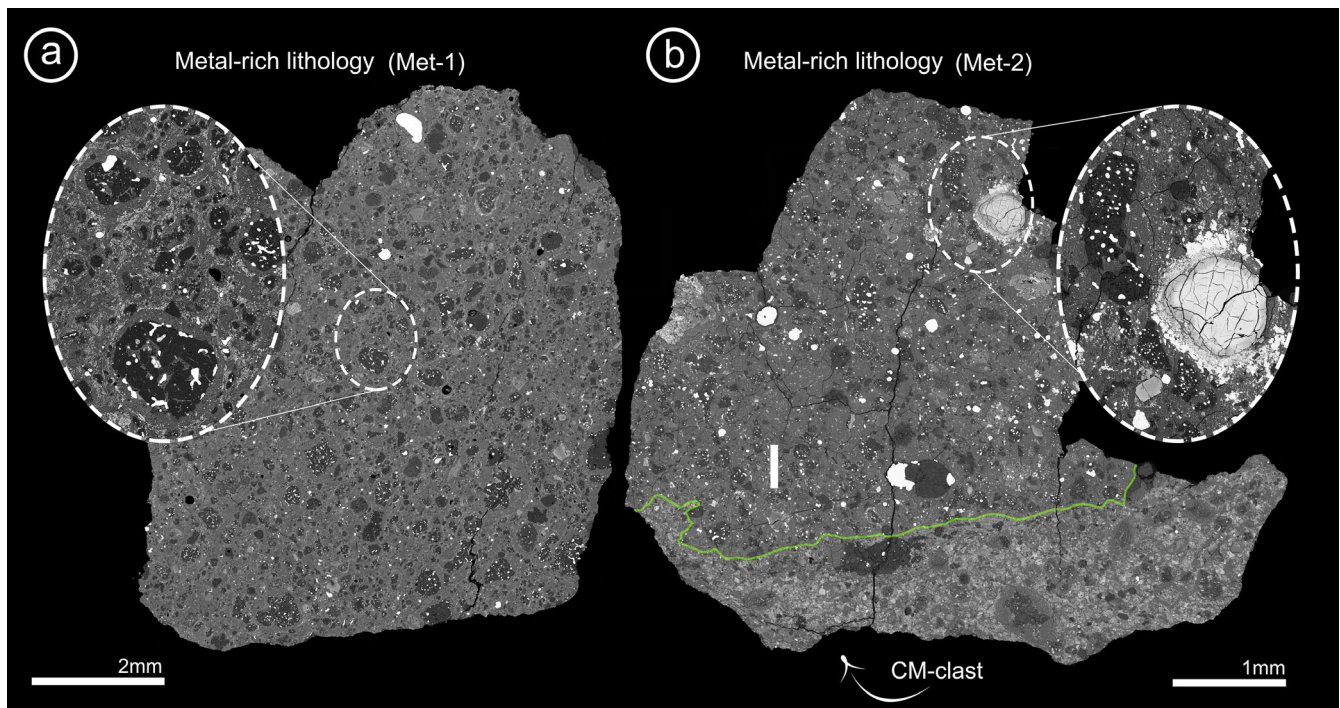


Fig. 3. Backscattered electron (BSE) images of the two thin sections PL19125 (a) and JSC-Mount3 (b). a) Met-1. b) Met-2. The line follows the boundary between the different lithologies.

The vast majority of clasts appear to be chondrule bearing, although there is one  $\sim 2.5$  mm dark homogenous clast in the JSC-40 sample (Fig. S1a in supporting information). This sample also contains an enormous multilayered, forsterite-rich chondrule nearly 6 mm in diameter with a relatively low X-ray attenuation consistent with its mineralogy (Fig. S1b). The UTA-2 sample is a single non-brecciated lithology with abundant, well-developed fine-grained rims around many chondrules (Fig. S1c).

### Aguas Zarcas Lithologies

We have noted five main lithologies in our Aguas Zarcas samples, including (1) Met-1: a unique metal-rich lithology (Figs. 2a, 3a, and 4a); (2) Met-2: a second metal-rich lithology (Fig. 3b) that is distinct from Met-1; (3) a brecciated CM lithology with clasts of at least three different petrologic subtypes, in section PL19111 (Fig. 4a); (4) a C1/2 lithology (Figs. 1b, 2b, and 4b); and (5) a C1 lithology (Fig. 5b). Met-1 is a new carbonaceous lithology and will be discussed in detail. The Met-2 lithology is very similar to Met-1 with respect to the metal content, but it is otherwise significantly different in texture and mineralogy (Fig. 6). We will also describe the C1/2 lithology and the C1 lithology in some detail, since they are very different compared to all other fragments. Several different CM

lithologies from Aguas Zarcas will be discussed for comparison.

### Petrography and Mineralogy

#### *Met-1 (Metal-Rich Lithology 1)*

The MS-2 fragment contains up to 10 vol% of typical CM lithologies (as clasts), but is mainly composed of the metal-rich lithology Met-1. Fe-Ni metal, Fe-Ni sulfides, olivine, pyroxene, and carbonate are the major phases in Met-1. In the three sections that we have prepared (PL19111, PL19112, and PL19125), two sections contain some CM clasts that we have also analyzed in order to make a comparison with this unusual metal-rich lithology (Fig. 4a).

#### *Silicates*

Olivine grains are found both in the chondrules and as clasts in the matrix, with similar compositions. The average compositions of olivine in both groups (chondrules and clasts) are  $Fa_{13.3 \pm 19.9}$  ( $n = 120$ ) varying between  $Fa_{0.5}$  and  $Fa_{75.5}$  (Fig. 7a). Isolated olivines in the matrix range in size from a few microns up to 100  $\mu m$  and have variable compositions from  $Fa_{0.8}$  to  $Fa_{52.7}$ . Zoned olivines are frequently found in the majority of chondrules. Their compositions range from Mg-rich cores ( $\sim Fa_1$ ) to Fe-rich rims ( $\sim Fa_{71}$ ; Fig. 8a). In addition, oscillatory-zoned olivine was observed

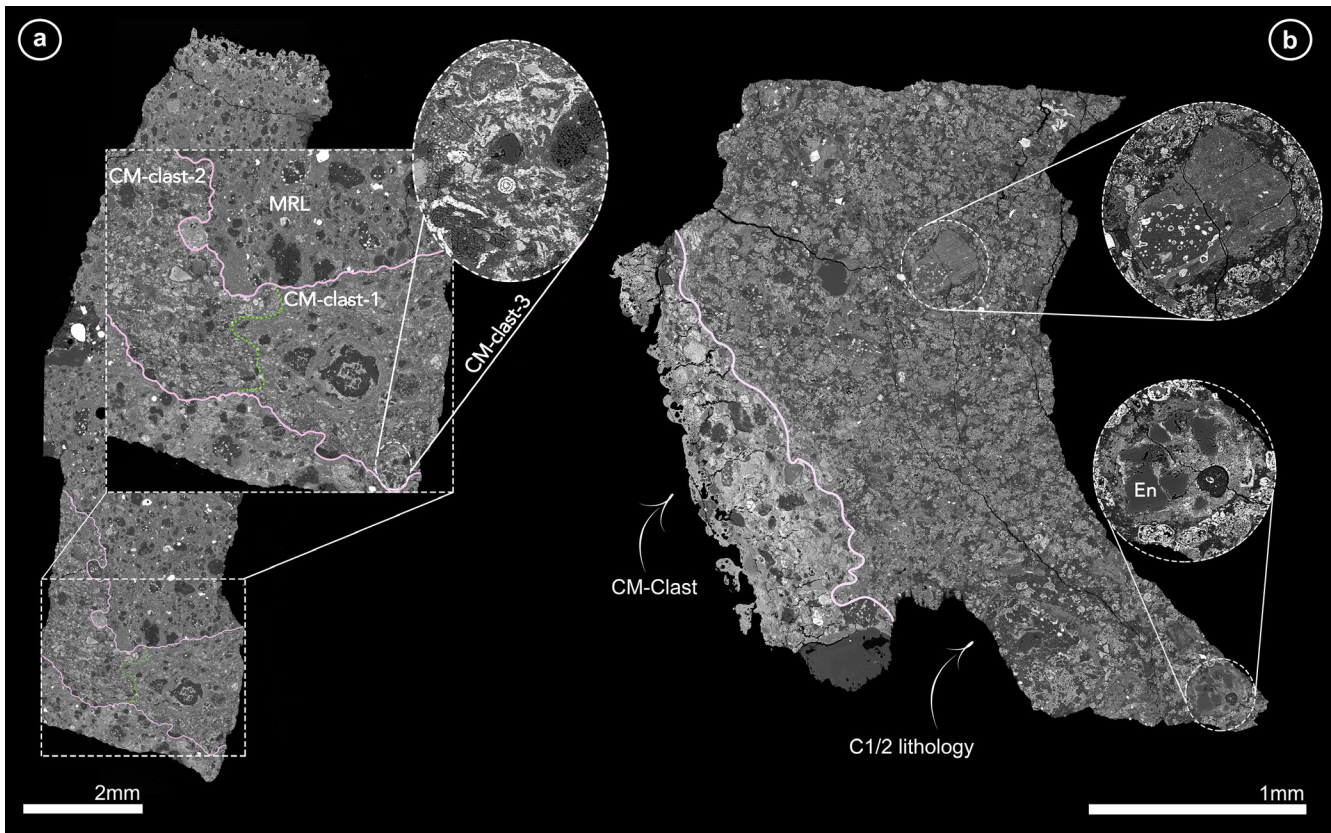


Fig. 4. Backscattered electron (BSE) images of the two thin sections PL19111 (a) and PL19145 (b), showing the brecciation of Aguas Zarcas. a) Met-1 (MRL) in the upper part and the brecciated CM chondrite with clasts of three CM subtypes in the lower part. b) C1/2 lithology (dark gray) and the CM lithology (light gray). The C1/2 lithology still contains some remnants of altered chondrules containing En-rich pyroxene (Fe<sub>10.8</sub>En<sub>60.5</sub> (lower case)). The lines demonstrate the boundaries between the different lithologies.

having an Fe-rich core ( $\sim$ Fa<sub>33</sub>) followed by an intermediate Mg-rich zone ( $\sim$ Fa<sub>22</sub>) and an outer Fe-rich rim with 37 mol% Fa (Fig. 8b).

Similar to olivines, the pyroxenes occur both in the chondrules and as grains in the matrix as well, but they are less abundant in the matrix compared to the abundance of isolated matrix olivine. Both low-Ca and Ca pyroxene occur. The average of low-Ca pyroxene compositions encountered within Met-1 in the chondrules and as isolated grains in the matrix is Fs<sub>2.4±3.3</sub> En<sub>95.1±4.9</sub> Wo<sub>2.5±2.4</sub> (Figs. 9a and 10). Low-Ca pyroxenes with an Fs content between 1 and 2 mol% are the most abundant pyroxenes in the metal-rich lithologies. The mean composition of diopside is Fs<sub>1.9±1.5</sub> En<sub>60.8±6.1</sub> Wo<sub>37.3±6.0</sub> (Fig. 10).

#### *Metal and Sulfide*

Metal and sulfides are the dominant opaque phases in Met-1, representing 3 vol% of Met-1 in all three sections. The metal is present in Met-1 as kamacite and taenite with modal abundance of 2.25 vol%. Their sizes range from a few  $\mu$ m up to 550  $\mu$ m (Fig. 11a). Most metals have

circular shapes; others are sometimes irregular in shape but have well-rounded edges. The predominant metal in Met-1 is kamacite with average Ni content of  $5.69 \pm 1.62$  wt%. Taenite occurs as exsolutions within some kamacite grains (Fig. 11b). The metal grains are sometimes speckled, containing small inclusions (Fig. 11d) or pores (observed in most of the metals). Inclusion diameters reach up to  $\sim 3$   $\mu$ m (Figs. 11b–d). The largest inclusion is an olivine (Fa<sub>41.6</sub>; Fig. 11d). Very often, Met-1 metal shows pre-terrestrial alteration (Fig. 11e), and one metal grain contains significant concentrations of Si (Fe = 90 wt%, Ni = 6 wt%, Si = 2 wt%, and Co = 2.3 wt%).

The sulfide minerals are pyrrhotite and pentlandite (Table 1) with a modal abundance of 0.75 vol% of the 3 vol% of the total volume of opaque phases. Pyrrhotite has an average Ni content of  $0.57 \pm 0.16$  wt%. Pentlandite contains an average of  $18.9 \pm 11.8$  wt% Ni and often occurs as exsolutions in pyrrhotite (Fig. 12a). In other cases, pentlandite forms large grains in sulfide aggregates (Fig. 12b) or exists as isolated grains. Some sulfides contain inclusions or cores of metal grains (Fig. 12c).



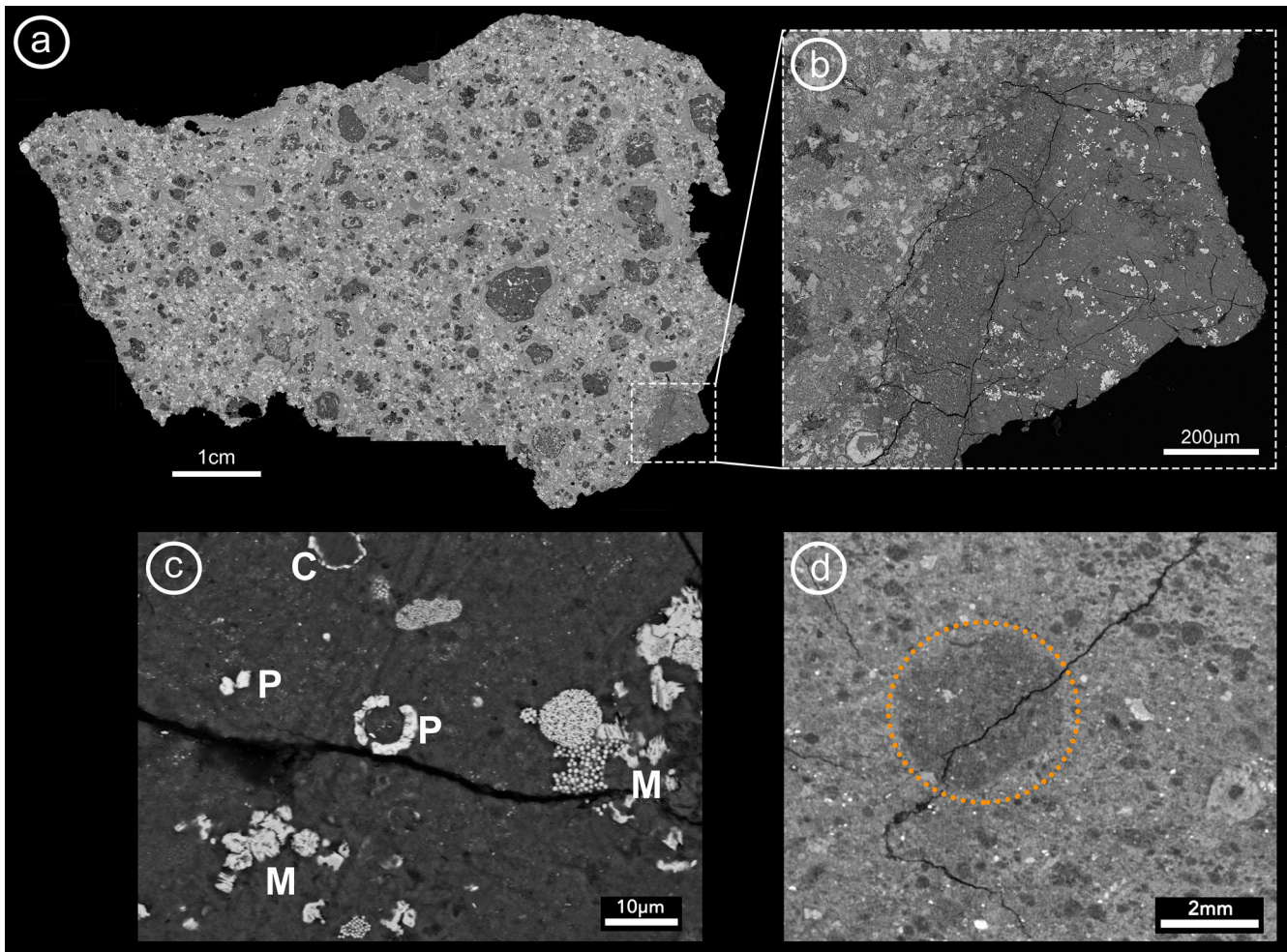


Fig. 5. Aguas Zarcas C1 lithology. a) BSE image of JSC-mount3, with square indicating position of C1 clast. b) Higher magnification BSE image of the C1 lithology shown in (a). c) BSE image of C1 lithology showing magnetite (M), pyrrhotite and pentlandite grains (P), a Ca-carbonate (C), all set within a very fine-grained matrix of phyllosilicate. d) One frame of XCT scan of sample JSC-60, with circle indicating probable cm-sized clast of the C1 lithology.

Concentric or cauliflower-like, polycrystalline sulfide–oxide aggregates are frequently observed in Met-1. They occur as solitary objects (Figs. 12d–f) or form layers on the surface of chondrules (Figs. 8b and 13c). The oxide phases are possibly magnetite or other Fe-rich phases associated with pentlandite, pyrrhotite, and Ca-phosphate. In some cases, relict metal is found in the center of the sulfide–oxide aggregates.

#### Other Phases

Other phases found in the Met-1 lithology are magnetite, chromite, and carbonate. Magnetite occurs in one section of Met-1, but its abundance is low. Magnetite morphologies range from platelets to framboids with variable grain sizes (Fig. 14). Chromite occurs in a chondrule within Met-1 as euhedral crystals up to 25  $\mu\text{m}$ . The chromite is essentially stoichiometric  $\text{FeCr}_2\text{O}_4$  with 57.9 wt%  $\text{Cr}_2\text{O}_3$  and 34.1 wt%  $\text{FeO}$ .

Carbonate occurs within the matrix and in the complex CAIs. The chemical composition is very close to that of pure  $\text{CaCO}_3$ . Raman spectra show that it is all calcite.

#### Chondrules

The chondrules in Met-1 are round to slightly irregularly shaped and have thick, fine-grained, rims (generally up to 160  $\mu\text{m}$  thick—sometimes even more). Porphyritic olivine chondrules (PO; Fig. 13) are the most abundant. Barred olivine (BO; Fig. 13a), porphyritic olivine–pyroxene (POP), and some radial pyroxene chondrules (RP; Fig. 13b) are also present. Most chondrules contain a high abundance of metal and sulfide grains either inside and/or at their edges (Figs. 8 and 13c–e) and are similar in texture to typical chondrules in CR2 chondrites (Weisberg et al. 1993), but on a very different size scale (cf. Table 2). Met-1 also contains some altered chondrules, which are embayed and partially replaced by phyllosilicates.

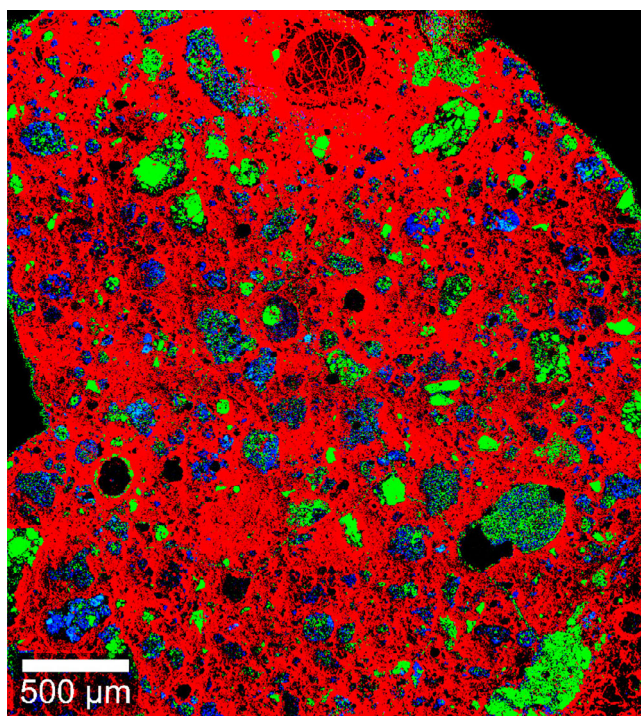


Fig. 6. Raman map of Met-2 showing the distribution of anhydrous silicates (olivine in green and pyroxene in blue) and phyllosilicates in the matrix (red).

Chondrule sizes vary from 14 to 800  $\mu\text{m}$ . The different methods used for size determination of chondrules within the Met-1 lithology give almost the same average chondrule size and model abundance: By means of optical microscopy, a mean size of 186  $\mu\text{m}$  with an abundance of 29 vol% was determined. Using BSE mosaic maps, the corresponding data are 149  $\mu\text{m}$  and 31.5 vol%. Details are given in Table 2. These data are clearly different to those of CM chondrites. The chondrules we measured within Banten, Maribo, and NWA 12651 have a mean chondrule size of  $\sim 270$   $\mu\text{m}$  (which is similar to that of Rubin and Wasson [1986] for Murray; Table 2). The data also show that Aguas Zarcas CM chondrite lithologies have a significantly lower chondrule abundance of approximately 20 vol% compared to the chondrule abundance within Met-1 (Table 2).

#### *Ca,Al-Rich Inclusions*

Two types of Ca,Al-rich inclusions (CAIs) can be distinguished within Met-1 (1) CAIs with a rounded shape and (2) irregularly shaped CAIs. The round CAIs can be subdivided into spinel-rich and hibonite-rich objects. The first type is usually small ( $\sim 80$   $\mu\text{m}$  in diameter) and the most abundant. CAIs of this type typically have spinel in their centers surrounded by an Al-rich diopside rim (Fig. 15h). In addition to the Al-rich

diopside rim, there is sometimes an outer rim of olivine (Fig. 15h). The second type of round CAIs (typically  $\sim 140$   $\mu\text{m}$  in diameter) is rich in hibonite having elongated and rounded grains (Fig. 15g). The irregularly shaped CAIs are large ( $\sim 500$   $\mu\text{m}$ ), very complex, and unusual in mineralogy. On average, they have a remarkably high abundance of calcite of  $\sim 53$  vol%. They are typically composed of calcite and spinel with some small perovskite grains (ranging from  $<2$  to 10  $\mu\text{m}$  in size). In some cases, minor fassaite was found enclosed within the spinel. These CAIs are typically surrounded by an Al-rich diopside rim of constant thickness (Figs. 15a–d).

#### *Fine-Grained Materials*

Met-1 contains different fine-grained components, including (1) fine-grained matrix, (2) rim material around coarse-grained components, and (3) individual fine-grained fragments (FGFs). In all cases, the fine-grained materials have EPMA analytical totals between 80 and 95 wt%, which reveal them to probably be phyllosilicates, although porosity must also contribute to the low totals. The matrix in Met-1 is heterogeneous, resulting from the presence of numerous voids/pores, oxides, carbonates, silicate, and metal grains. The mean total of  $87.3 (\pm 4.0)$  wt% is the same as the averages we obtain for the matrix within the different CM lithologies in Aguas Zarcas. The composition of the matrix is similar to that of a serpentine and in agreement with that of other Aguas Zarcas CM lithologies (Figs. 16a and 17). Chondrules, CAIs, and some metal and silicate grains have fine-grained rims (FGRs; Metzler et al. 1992). The boundaries between the rims and matrix are very clear, often separated by tochilinite–cronstedtite intergrowths (TCIs). The overall composition of the FGRs is comparable to that of the matrix of Met-1.

TCIs in Met-1 consist of aggregates of intergrown platelets and acicular fibers of cronstedtite and tochilinite typically 1–2  $\mu\text{m}$  in width and 3–5  $\mu\text{m}$  in length (Fig. 18a), similar to the “PCP type-1 objects” of Tomeoka and Buseck (1985), which were properly identified as intergrowths of “serpentine” and tochilinite by Mackinnon and Zolensky (1984). The analyses revealed variable amounts of S and Si, but relatively constant Fe concentration with (locally) some elevated Ca contents possibly due to the occurrence of minor carbonate. Within the S/SiO<sub>2</sub> versus “FeO”/SiO<sub>2</sub> diagram (Fig. 19), the data of individually analyzed TCIs show significant scatter. Considering the mean TCI compositions of the individual clasts shown in Fig. 18 (Met-1, CM-clast1, CM-clast2, CM-clast3, and C1/2 lithology), clear differences concerning the degree of aqueous alteration are obvious. Considering the average compositions of the Met-1 lithology (Table 3), the petrologic subtype relating to the degree of aqueous



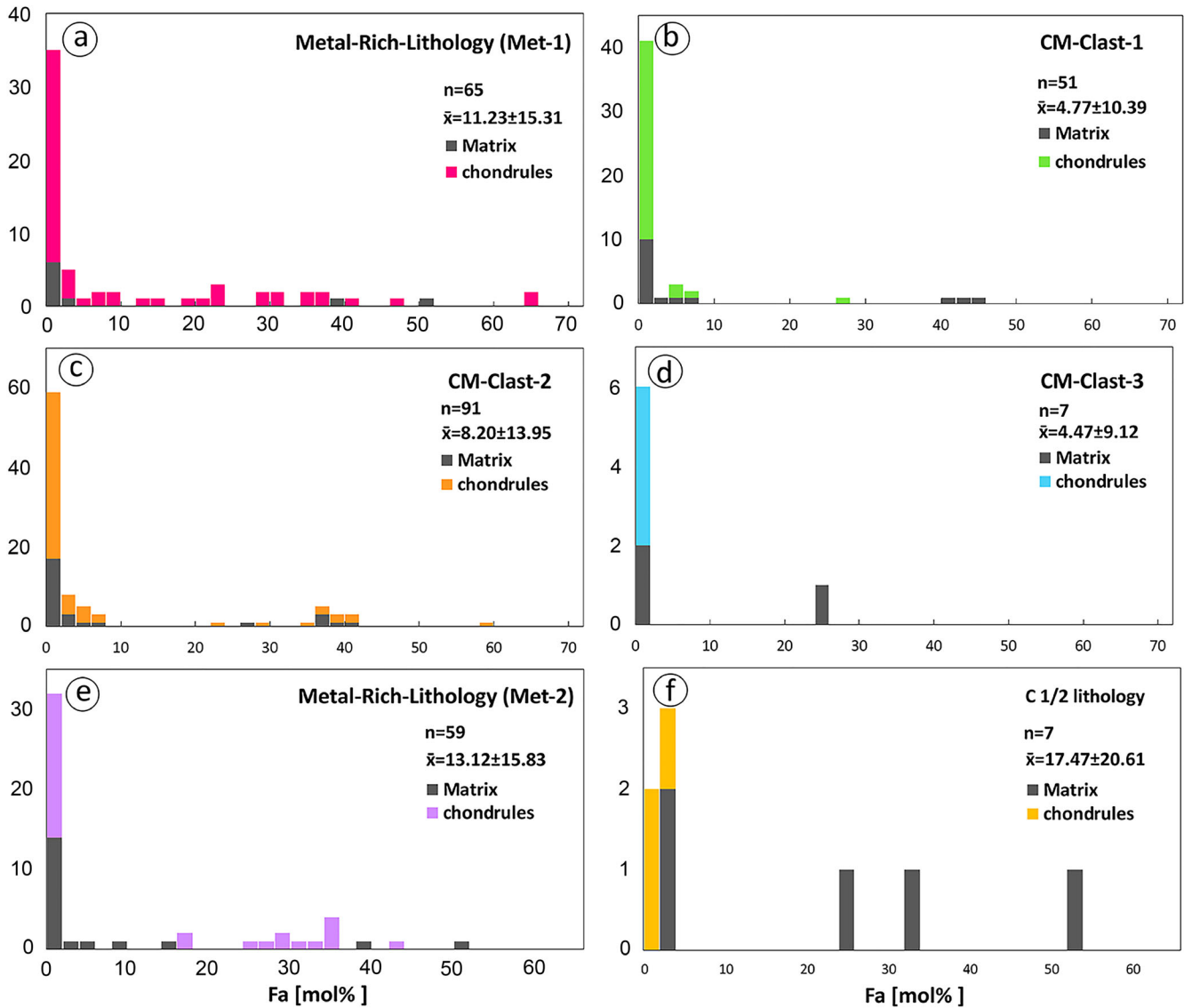


Fig. 7. Histogram showing the distribution of the Fa-contents of individual olivines present in chondrules and as clasts in the matrix of Met-1 (a), the three CM-clasts within Met-1 (b-d), Met-2 (e), and the C1/2 lithology (f).

alteration can be defined as 2.5 for Met-1, which is inconsistent with the previous observation. In other words, the type of lithology with the highest abundance of metal (Met-1) shows the second lowest “FeO”/SiO<sub>2</sub> ratio, indicating a high degree of aqueous alteration. This inconsistency will be discussed in more detail below.

The last fine-grained components described are the fine-grained fragments (FGFs). These fragments are also analyzed in order to compare them with the compositions of the matrix and rims. They typically have μm-sized grains, similar to matrix and rims, but contain some slightly larger metal and sulfide grains. The FGFs are found in Met-1 as well as in one CM

lithology (CM-clast2) and are very similar in texture and mineralogy. However, chemical analyses reveal significant differences, which are shown in Fig. 16b. They are richer in Fe within Met-1 than the latter, which is richer in Si. In addition, the FGFs have numerous fractures that do not extend into the matrix. Similar observations can be made regarding the chondrule rims; these observations are very common in heated CM chondrites (Hanna et al. 2020). Comparing the compositions of the FGFs found in the two different lithologies with typical rim compositions (see above), the FGF in Met-1 and the FGF in CM-clast2 plot in the same compositional field as the rim compositions of Met-1 and CM-clast2. The

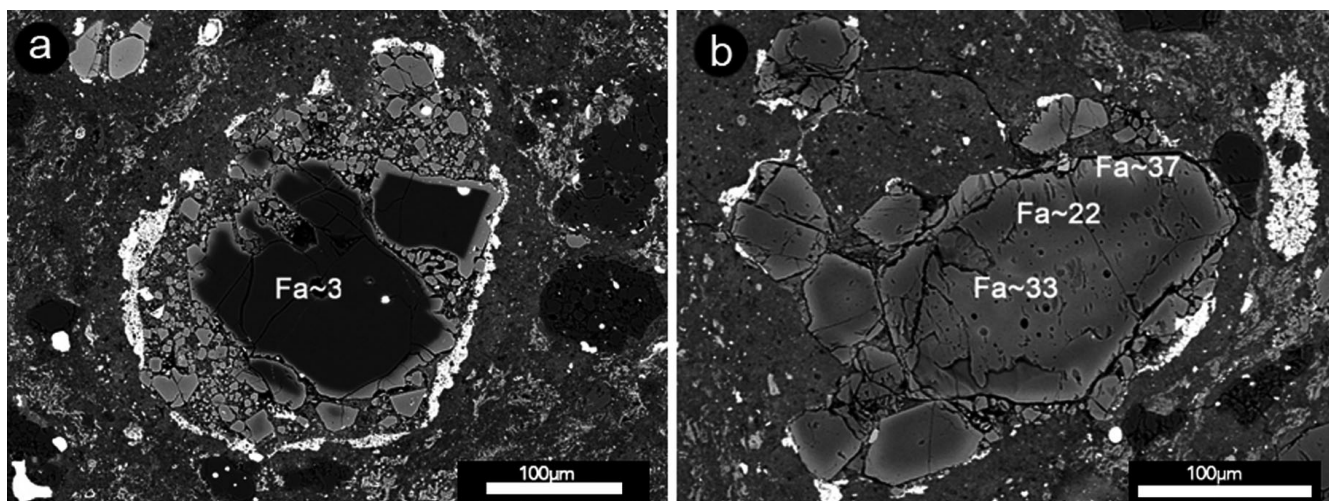


Fig. 8. Chondrules containing zoned olivines within Met-1. a) Olivine with Mg-rich cores and Fe-rich rims. b) Oscillating-zoned olivine with an Fe-rich core, Mg richer intermediate area, and an Fe-rich outer rim. BSE images.

compositional and textural (i.e., fractures) similarity between the FGRs and FGFs suggests that the FGFs are likely the edges of FGRs isolated by 2-D sectioning (e.g., Hanna and Ketcham 2018). In Fig. 17, the compositional variations between matrix material of Met-1 from Aguas Zarcas are compared to those of CM and CR chondrite matrix (Zolensky et al. 1993; Weisberg and Huber 2007). The chemical composition of matrix plots in between the two fields defined by CM and CR chondrite matrix.

### *Met-2 (Metal-Rich Lithology 2)*

Met-2 is the second unusual, metal-rich lithology found in Aguas Zarcas. This lithology shows a very close similarity to Met-1, but it is clearly distinct based on its higher metal (plus sulfide) abundance and the lack of fine-grained rims around coarse-grained components, which are abundant in Met-1 (Fig. 3). Met-2 is mainly composed of metal, sulfides, olivine, pyroxene, and carbonate.

Olivine and pyroxene were found in the chondrules and as isolated grains in the matrix, with both populations having similar composition. The olivine has similar Fa contents and grain sizes as in Met-1. Fa content ranges from  $Fa_0$  to  $Fa_{60}$ , with a pronounced peak at  $Fa_1$  (Fig. 7e). The average of low-Ca pyroxene compositions is also identical to that of Met-1, and has a similar mean Fs content of  $\sim 2$  mol% (Figs. 9e and 10). The metals and the sulfides are likewise dominant here, but more abundant than in the Met-1 lithology. In Met-2, their abundance is 5 vol%, compared to the 2.25 vol% in Met-1, and this is one criteria that distinguishes the two metal-rich lithologies. As for Met-1, the metal in Met-2 is a mixture of kamacite and taenite and has

similar morphologies and characteristics, although their sizes are smaller in Met-2 (by about 50%), ranging from a few  $\mu\text{m}$  up to 250  $\mu\text{m}$  (Fig. 11e).

The chondrules are round to slightly irregularly shaped, with 20 vol% as the modal abundance and 136  $\mu\text{m}$  ( $n = 166$ ) in mean diameter. However, a substantial difference between Met-1 and Met-2 is the absence of fine-grained rims around coarse-grained components in Met-2, which are very well developed and thick within Met-1.

As for the CAIs, the elementary maps show some Al-rich phases that are probably related to CAIs, but no fully intact CAIs are present in the Met-2 section. However, given the small sampling volume, no conclusive statement about the abundance of CAI can be made.

All three FIB sections from matrix of the Met-2 lithology show similar mineralogy. The matrix is dominated by poorly crystalline phyllosilicate material whose morphology ranges from spongy to thin fibers up to larger crystallites (see Fig. 20). Although the forms of phyllosilicates are typical, no 0.7 (serpentine) or 1.4 nm (smectite) lattice fringes are visible. This situation is typical for meteoritic phyllosilicates heated to 450–700 °C (see Tonui et al. 2014). At lower temperatures, interlattice serpentine fringes survive, and at higher temperatures, the phyllosilicates recrystallize into fine-grained anhydrous phases (e.g., Nakamura 2005; Tonui et al. 2014; Ebert et al. 2019b). EPMA analyses of the matrix yielded few acceptable compositions because of numerous included submicron-sized mineral phases. Set within the poorly crystalline phyllosilicates are submicron-sized Fe-Ni sulfides, spinel, and lesser magnetite and Fe carbides. It is

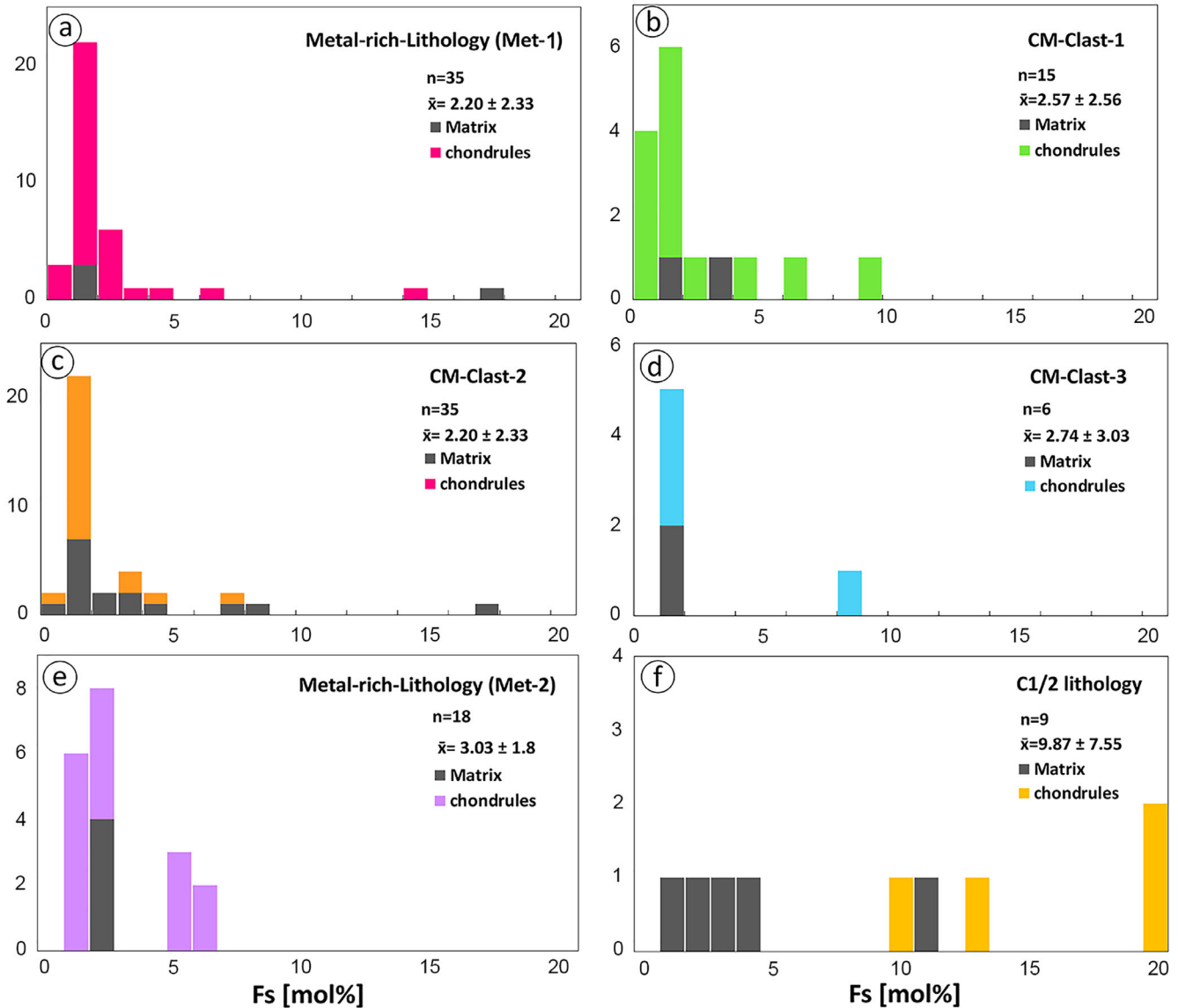


Fig. 9. Histogram showing the distribution of the Fs contents of individual Ca-low-pyroxene present in chondrules and as clasts in the matrix of Met-1 (a), the three CM clasts within Met-1 (b-d), Met-2 (e), and the C1/2 lithology (f).

unusual for abundant spinel and carbides to be present in meteoritic phyllosilicate (Zolensky et al. 1993). Large grains of diopside/endiopside and large phyllosilicate crystals are also present (Fig. 20).

### CM Lithologies

As already mentioned, we have also analyzed CM lithologies in Aguas Zarcas in order to compare them with the other, more unusual lithologies that are present. We therefore investigated three clasts found in section PL19111 (CM-clast1, CM-clast2, CM-clast3), which are associated with Met-1 (Fig. 4a).

The olivine in CM-clast1 and CM-clast3 has very similar mean Fa contents ( $Fa_{4.7\pm 10}$  and  $Fa_{4.5\pm 9}$ ,

respectively; Figs. 7b and 7d), while olivine in CM-clast2 has an average of  $Fa_{8.2\pm 13}$ , which is higher compared to those of the other two CM clasts (Fig. 7c). For the pyroxene, the three CM clasts have similar mean Fs contents of  $\sim 2$  mol% and are similar to those of the Met-1 lithology (Figs. 9 and 10). The CM clasts also contain some small grains of kamacite (Fig. 21). CM-clast1 and -clast2 contain both pentlandite and pyrrhotite. CM-clast3 contains only pyrrhotite, sometimes showing a “bull’s-eye” morphology (Fig. 12e).

In regard to fine-grained materials, the matrix in the CM clasts is heterogeneous, resulting from the presence of numerous voids/pores, oxide, carbonate,

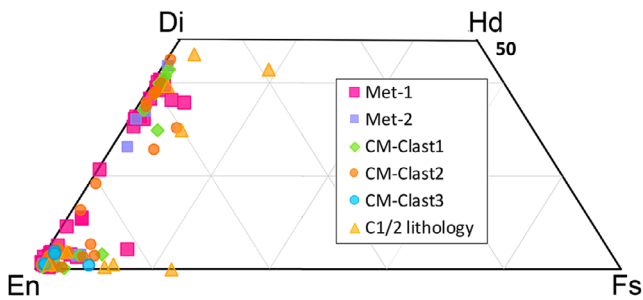


Fig. 10. Compositions of pyroxene grains in Met-1, Met-2, the C1/2 lithology, and the different CM clasts shown in Fig. 4a.

silicate, and metal grains. The mean total of  $87.3 (\pm 4.0 \text{ wt}\%)$  is the same as the averages for the matrix within the Met-1 lithology. The composition of the matrix is similar to that of serpentine (Figs. 16a and 17). Rims in the three CM clasts have different compositions. The composition of rim material in CM-clast1 plots in the same field as the rims in the Met-1 lithology. Both are FeO-rich, while the rims within CM-clast2 and CM-clast3 plot in the same field but at somewhat higher  $\text{SiO}_2$  values (Fig. 16b). TCIs in the three clasts show slightly different compositions. In an  $\text{S}/\text{SiO}_2$  versus “FeO”/ $\text{SiO}_2$  diagram (Fig. 19), the data of individually

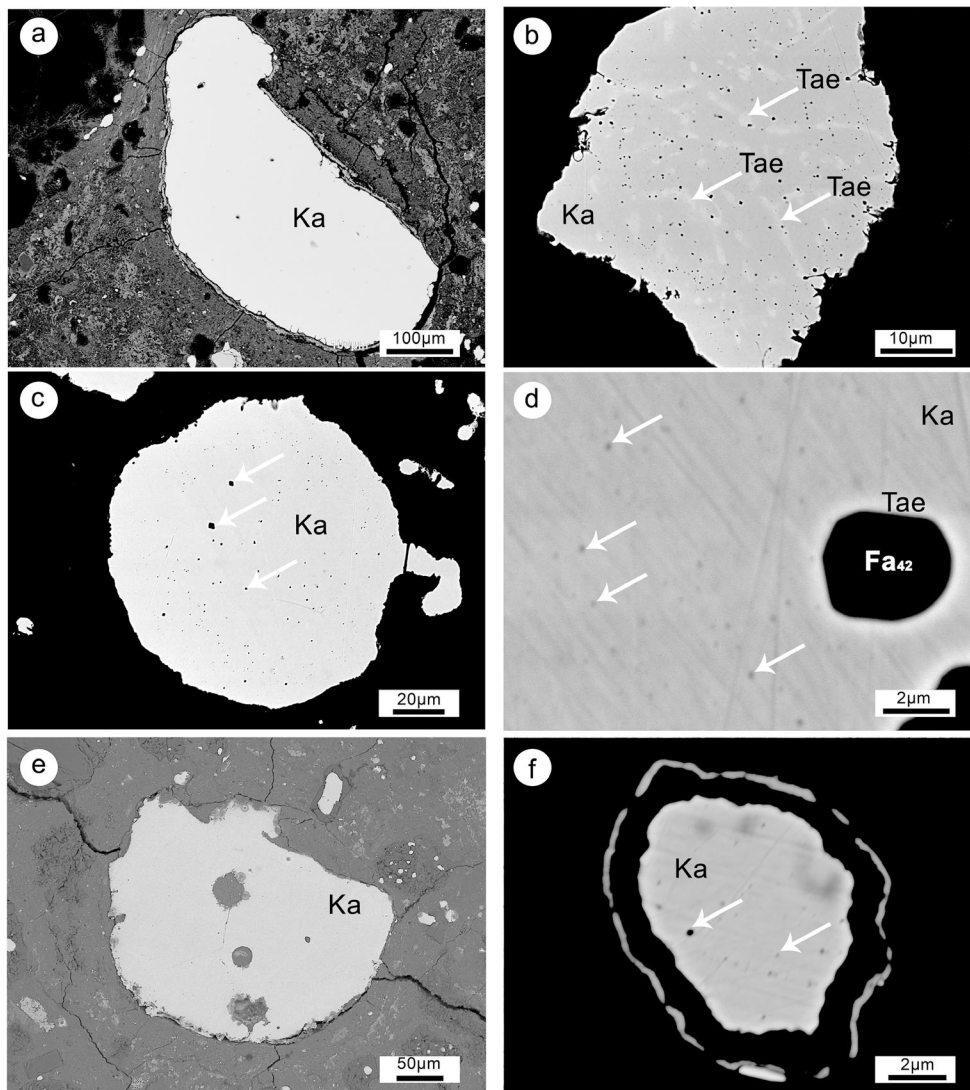


Fig. 11. Backscattered electron images of individual metal grains showing the variety of morphologies found in the Agua Zarcas. a) Large kamacite (Ka) grain of  $\sim 550 \mu\text{m}$  in the Met-1. b) Taenite (Tae) occurs as exsolutions in kamacite. Pores occur in the kamacite as well as in the taenite within the Met-1. c) Large circular grain of kamacite containing pores indicated by white arrows in the Met-1. d) High magnification of the image presented in (c) showing black dots in kamacite and olivine ( $\text{Fa}_{42}$ ). e) Large kamacite (Ka) grain within the Met-2 containing pores filled by matrix material. f) Kamacite (Ka) within the C1/2 lithology showing black dots, surrounded by a thin alteration rim.



Table 1. Mean chemical composition of metals and sulfides within different lithologies of the Aguas Zarcas meteorite. All data in wt%; microprobe and normalized to 100%.

	n	S	Fe	Ni	Co	Total
<b>Met-1</b>						
Pyrrhotite	10	38.08 ± 0.23	61.04 ± 0.17	0.57 ± 0.16	0.31 ± 0.13	100
Pentlandite	13	34.78 ± 2.18	45.45 ± 9.97	18.86 ± 11.81	0.92 ± 0.30	100
Kamacite	45	0.03 ± 0.02	93.66 ± 1.64	5.69 ± 1.62	0.62 ± 0.10	100
Taenite	4	0.15 ± 0.23	71.23 ± 16.40	27.27 ± 15.75	1.36 ± 0.60	100
<b>CM-clast-1</b>						
Pentlandite	1	33.53	31.03	34.13	1.30	100
Kamacite	4	0.02 ± 0.01	92.55 ± 1.66	6.74 ± 1.52	0.68 ± 0.15	100
<b>CM-clast-2</b>						
Pentlandite	7	34.25 ± 1.63	41.68 ± 11.14	23.21 ± 12.33	0.86 ± 0.33	100
Kamacite	5	0.02 ± 0.03	93.83 ± 0.43	5.46 ± 0.35	0.68 ± 0.17	100
Pyrrhotite	1	38.08	61.33	0.41	0.17	100
<b>CM-clast-3</b>						
Pyrrhotite	3	38.11 ± 0.62	60.86 ± 0.33	0.68 ± 0.21	0.35 ± 0.16	100
<b>C1/2 lithology</b>						
Kamacite	12	0.03 ± 0.03	94.23 ± 2.05	5.61 ± 1.29	0.10 ± 0.08	100
Pentlandite	14	34.8 ± 2.08	42.9 ± 10.33	21.2 ± 11.88	0.4 ± 0.323	100

analyzed TCIs show significant scatter. Figure 18a shows the different morphologies of TCIs of three clasts (b, c, and d). The mean TCI compositions of the individual clasts are shown in Fig. 19. Considering the average TCI compositions of all three different clasts (Table 3), CM-clast1 and CM-clast2 appear to share the petrologic subtype 2.6, while CM-clast3 is the least altered and is assigned to petrologic subtype 2.8 (compare Rubin et al. 2007; Lentfort et al. 2020).

### C1/2 Lithology

The C1/2 lithology contains abundant (~80 vol%) matrix phyllosilicates (cronstedtite + serpentine) with minor amounts of magnetite (<1 vol%), sulfides (<2 vol%), olivine and low-Ca pyroxene (each ~3 vol%), and calcite (<2 vol%) that are frequently enclosed within cronstedtite-rich TCIs and some metal grains.

Some olivine grains were found in the C1/2 lithology as grains in the matrix and also within the relict chondrules. These grains range from 10 to 160 µm in size with a relatively homogeneous chemical composition (mean:  $\text{Fa}_{2.1 \pm 2.1}$ ;  $n = 7$ ). Some pyroxene grains are also present. Low-Ca pyroxene in the matrix appears to be homogenous (mean  $\text{Fs}_{3.2 \pm 1.84}$   $\text{En}_{93.8 \pm 1.32}$   $\text{Wo}_{2.92 \pm 0.57}$ ). One Ca-rich pyroxene was also found within a relict chondrule ( $\text{Fs}_{10.8}$   $\text{En}_{60.5}$   $\text{Wo}_{28.7}$ ).

Regarding metallic phases, this lithology contains only kamacite. Similar to kamacite in the Met-1 lithology, the kamacites in the C1/2 lithology contain black dots that may represent pores (Fig. 11f). Metal frequently shows indications of pre-terrestrial alteration. Pentlandite is the only sulfide observed having a very

variable Ni concentration ( $\text{Ni} = 20.6 \pm 11.9$  wt%). Most pentlandite in this lithology appears to be altered or has been transformed into secondary alteration products. Some of them have kept similar features and textures of alteration as found in Met-1 (Fig. 12f). The C1/2 lithology contains strongly altered chondrules (Fig. 13f), some containing relic grains of olivine and/or pyroxene (together 15 vol%) and having an  $\text{SiO}_2$ - and S-rich mesostasis. The sizes of relict chondrules within this lithology range from 70 to 650 µm (average: 256 µm).

The C1/2 lithology contains one type of CAI that is irregularly shaped (~60 µm) and mainly composed of spinel. The representative CAI shown in Figs. 15e and 15f also contains small grains of perovskite and a matrix of phyllosilicate surrounded by an Al-rich diopside rim (Figs. 15e and 15f). It is very similar to the second type of CAI found within Met-1, except that it does not contain calcite.

The matrix is very complex, consisting of two different types (1) bright, Fe-rich matrix and (2) dark, S-rich matrix. Both have similar abundances of MgO and  $\text{SiO}_2$  (Figs. 16 and 18f). Fine-grained rims surround relict chondrules, TCIs, CAIs, and mineral clasts. Their compositions plot directly on the bright matrix of the same lithology (Fig. 16b).

The C1/2 lithology mainly consists of different types of TCIs (~70 vol%). The most abundant type consists of acicular fibers (Fig. 18f) rich in Fe, often associated with calcite. The second type (appearing darker in BSE images) is rich in S and typically occurs within altered chondrules. Cronstedtite appears to be

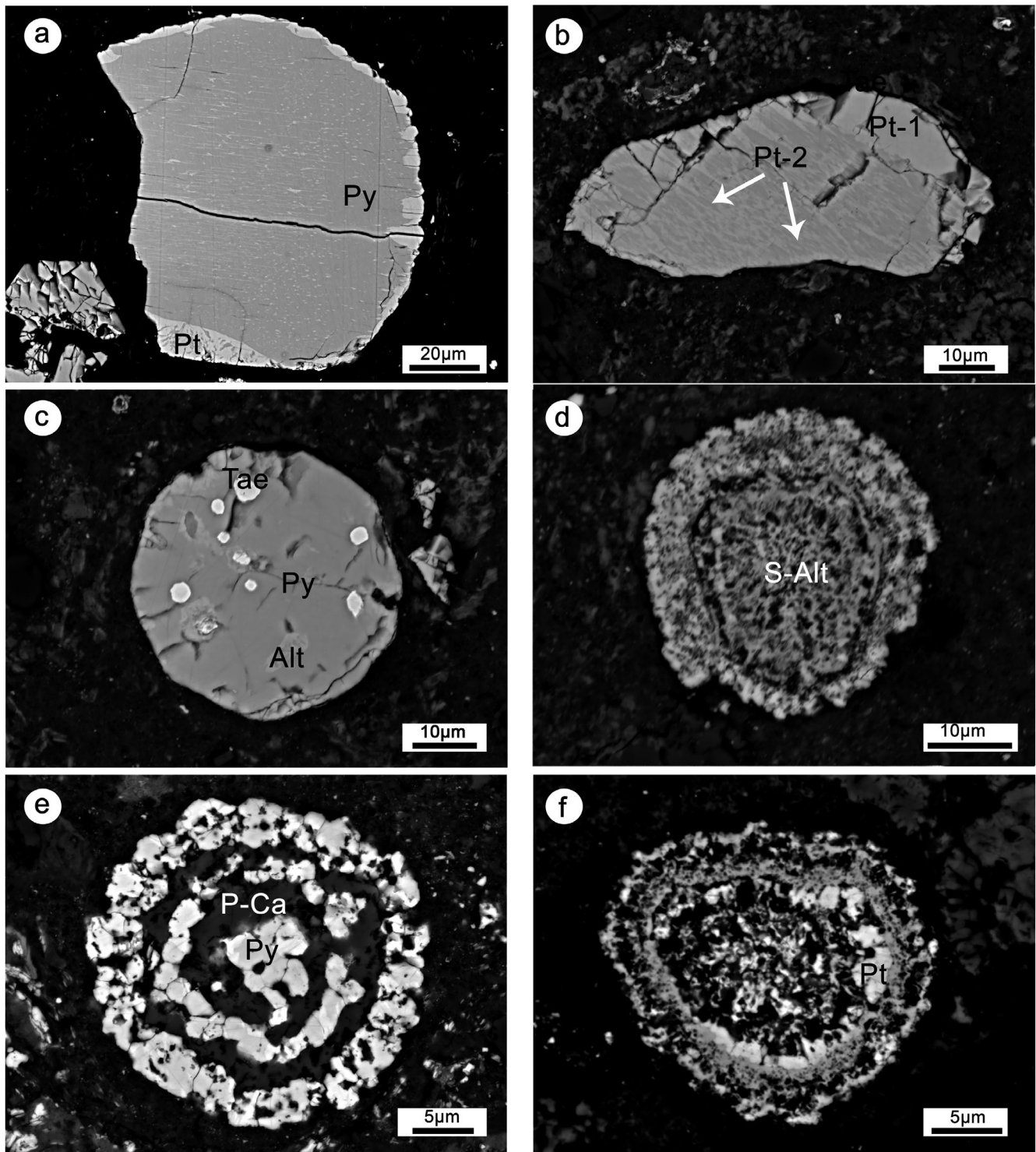


Fig. 12. Backscattered electron images of individual sulfide-rich objects. a) Exsolutions of pentlandite (light phase, Pt) in pyrrhotite (Py) within the Met-1. b) Pentlandite (Pt-1) occurs as exsolutions in another pentlandite of different composition (Pt-2) in the Met-1. c) Sulfide (pyrrhotite; Py) containing taenite inclusions (Tae) within the Met-1. d) Concentric assemblage. Light gray phases are sulfides and darker gray phases are oxides in the Met-1. e) Pyrrhotite (Py) in the CM-clast-3 showing a “bull’s-eye” morphology exhibiting a distinctive core and shells separated by a Ca,P-rich phase (P-Ca, probably phosphate). f) Altered pentlandite (Pt) within the C1/2 lithology showing an unusual, porous texture.

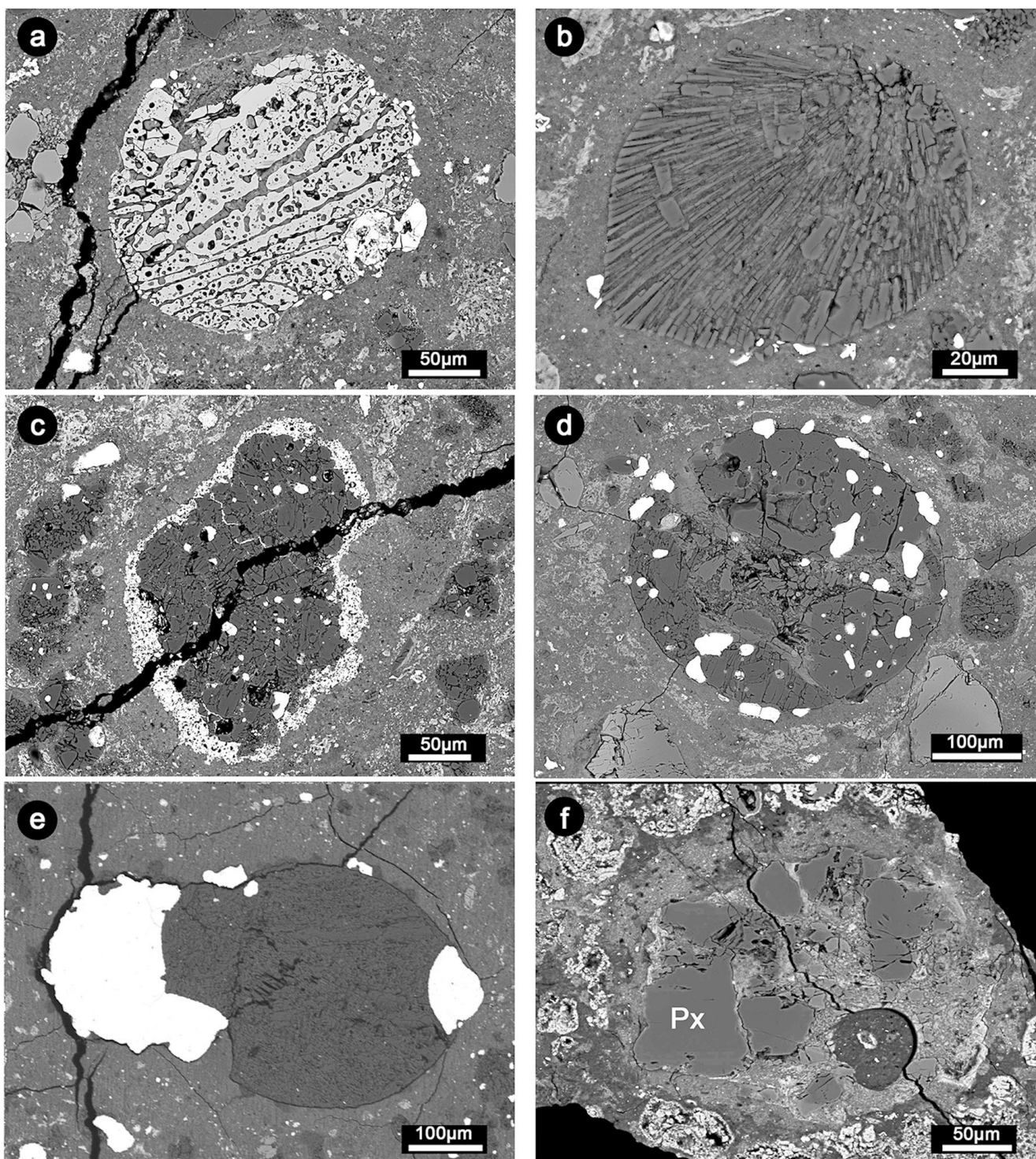


Fig. 13. Backscattered electron images of chondrules within Met-1. a) Barred olivine (BO) chondrule (type IIA). b) Radial pyroxene (RP) chondrule. c) Porphyritic olivine-pyroxene (POP) chondrule surrounded by sulfide. d) POP chondrule surrounded by metal with some metal grains inside as well. e) Chondrule mainly consists of olivine, containing large metal grains within the Met-2. f) Altered chondrule within the C1/2 lithology mainly consisting of pyroxene.

the dominant phase. In the  $S/SiO_2$  versus “FeO”/SiO<sub>2</sub> diagram (Fig. 19), the C1/2 lithology shows a low petrologic subtype of 2.2 indicating a high degree of

aqueous alteration. But to check this, we analyzed the TCIs of the Moapa Valley CM1 chondrite. Moapa Valley exhibited a petrographic subtype identical to that

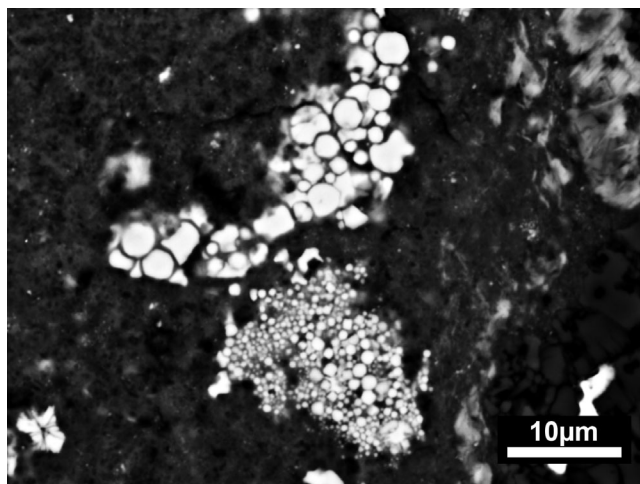


Fig. 14. Magnetite within Met-1 lithology. Image in backscattered electrons (BSE).

of C1/2, which is 2.2 (Fig. 19). These results will be interpreted in the Discussion section.

### C1 Lithology

The C1 lithology was found in pre-rain samples CR19.19 and CR19.29 and at least three additional pieces of this same lithology appear to be present in JSC-60 (a post-rain sample), as revealed by XRCT (Fig. 5d), although this latter identification requires verification after the stone is cut. The maximum size of clasts of the C1 lithology in our samples is 1 cm. This lithology contains abundant matrix phyllosilicates, magnetite, sulfides, and some Ca-carbonate grains.

The bulk composition of the phyllosilicates in this lithology lies between that of serpentine and saponite, but closer to the latter as is the case for CI and CR chondrites (Fig. 5). However, in contrast to phyllosilicates in CI and CR chondrites, the FeO content is quite uniform (11–20 wt% FeO). This composition is very similar to that of the phyllosilicates in Almahata Sitta 91A, a C1 chondrite lithology of very unusual isotopic composition (Goodrich et al. 2019). Analytical EPMA totals for the phyllosilicate are low (65–86 wt%), as expected for fully hydrated material.

Abundant framboidal to plaquette magnetites are set within the “phyllosilicates” (Fig. 22) as well as fine-grained pyrrhotite and pentlandite. The latter two exhibit their typical exsolution texture (Fig. 5c). The sub- $\mu\text{m}$  grain size of matrix phyllosilicates defies highly accurate EPMA analysis. Some Ca-carbonate grains are also present, sometimes rimmed by sulfides or magnetite, as shown in Fig. 5c. No anhydrous silicates, chondrules, CAI, or pseudomorphs after these objects are evident. However, the total amount of material

from this lithology—observed until today—is very limited. Thus, coarse-grained components could be present elsewhere, though it would probably be in very low abundance.

### Oxygen Isotopes

We measured O isotopes of five samples of Aguas Zarcas: Met-1 (from MS-2), chondrule-poor CM, a chondrule-rich CM, CM-clast (from Münster sample), and the C1/2 lithology (from CR19.19). The results are given in Table 4 and plotted in Fig. 22. All compositions fall below the terrestrial fractionation line (TFL). Met-1 plots significantly away from the CM field, below the CCAM line with ( $\delta^{18}\text{O} = 3.8$ ;  $\delta^{17}\text{O} = 2.7$ ). The other lithologies all plot in the field of CM chondrites, with the C1/2 lithology having a mean value similar to the chondrule-poor Aguas Zarcas CM lithology,  $\delta^{18}\text{O} = 10.8$ ;  $\delta^{17}\text{O} = 3.2$ ; and  $\delta^{18}\text{O} = 10.6$ ;  $\delta^{17}\text{O} = 3.5$  successively.

## DISCUSSION

### Classification of Unusual Lithologies in Aguas Zarcas

The Aguas Zarcas meteorite has been officially classified as a CM2; however, the meteorite is more complex than this, consisting of several different lithologies. Besides the CM lithologies that are similar to those previously described from brecciated CMs (e.g., Bischoff et al. 2006, 2017; Lindgren et al. 2013; Zolensky et al. 2015, 2017; Metzler et al. 1992; Lentfort et al. 2020), four other unusual lithologies are present in significant abundance, classified here as (1) Met-1, (2) Met-2, (3) a C1/2 lithology, and (d) a C1 lithology.

#### Met-1

In terms of petrography, Met-1 shows similarities with CM and CR chondrites. Although the silicates and phyllosilicates within Met-1 show similar compositions as those of CM chondrites (Figs. 7, 9, 10, 16, and 17; Zolensky et al. 1993, 1997), chondrules are frequently surrounded by metal (Fig. 13d), which is a common feature of CR chondrites (Bischoff 1992; Bischoff et al. 1993; Weisberg et al. 1993). The mean chondrule size of about 160  $\mu\text{m}$  (Table 2) is clearly different from CM chondrites ( $\sim 270 \mu\text{m}$ ; Rubin and Wasson 1986). The data also show that CM chondrites have a significantly lower though widely varying chondrule abundance of approximately 20 vol% compared to the abundance within Met-1 (30 vol%). However, CR chondrites have mean chondrule diameters of  $\sim 700 \mu\text{m}$  and chondrule abundance of  $\sim 55$



Table 2. Mean apparent chondrule diameters (mm) and chondrule abundances (vol%) in the Met-1 lithology and in some CM chondrites for comparison.

Sample	Reference	Section size (mm)	Area (mm <sup>2</sup> )	n	From-to (mm)	Chondrules mean diameter	STD	Chondrules (vol%)	Methods
Met-1	PL19125	8 × 6.7	53.6	721	0.014–0.802	0.136	0.118	32	BSE map
Met-1	PL19125	8 × 6.7	53.6	218	0.040–0.802	0.207	0.142	28	Microscope transmitted light
Met-1	PL19112	7 × 3.3	23	116	0.036–0.672	0.162	0.060	30	Microscope reflected light
Met-1	PL19111	9.5 × 3	28.5	145	0.023–1.38	0.162	0.196	31	BSE map
Met-2	JSC-Mt3	4.6 × 2.6	12	166	0.041–0.635	0.136	0.077	20	BSE map
C1/2 lithology	PL19149	3.6 × 1.2	4.2	13	0.070–0.650	0.256	0.152	15	BSE map
Banten-CM	PL93094	7.7 × 6.8	52.4	77	0.061–1.424	0.284	0.228	21	Microscope transmitted light
Maribo-CM	PL09089	5.6 × 16	90	88	0.061–0.714	0.268	0.160	20	Microscope transmitted light
NWA12651-CM	PL17261	18 × 8.7	157	165	0.046–1.302	0.275	0.218	20	Microscope transmitted light
Murray CM	USNM	<sup>a</sup>	–	–	–	0.270	–	20	Microscope transmitted light
Renazzo-CR	AMNH	<sup>b</sup>	–	–	–	0.700	–	55	Polished thin sections (PTS)

Met1 and Met-2: Metal-rich lithologies; n: number of chondrules analyzed.

<sup>a</sup>20 thin sections of Murray (USNM 1) with a total surface area of about 16 cm<sup>2</sup> (Rubin and Wasson 1986).

<sup>b</sup>CR data from Weisberg et al. (1993).

vol% (Weisberg et al. 1993), which are distinctly different from Met-1.

The O-isotope composition of the Met-1 (Fig. 22) plots far from the CM area, which argues against a direct relation to CM chondrites. This contention is supported by the Ti isotope composition, which suggests a closer relationship with CR chondrites (Kerraouch et al. 2020) despite differences in chondrule sizes and abundance. Thus, the Met-1 lithology is distinctly different from CM chondrites as well as from CR chondrites, and probably derives from a previously unsampled parent asteroid.

### Met-2

The chemical data of olivine in Met-2 show similarities with those of olivine in Met-1, and are typical for olivine in most CM and CR chondrites (Frank et al. 2014). Carbon, nitrogen, and hydrogen isotopic values are also within the range of CM chondrites (Kerraouch et al. 2020). Without data for oxygen isotopes, it is impossible to suggest a CM affinity for Met-2, but we tentatively propose that the Met-2 lithology could be CM-related.

Element mapping of JSC-mount3 (Fig. 23b) revealed a pronounced elevation in the abundance of metal as well as sulfides in Met-2, but aside from this, Met-2 (as well as Met-1) appears to be very similar to CMs with respect to the size and abundance of chondrules (136 μm and 20 vol%, respectively). A fine-grained, plagioclase-rich CAI is also present of Met-2 (Fig. 23b), which also supports a possible relationship with CM chondrites or similar

environment of formation. An unusual feature is the apparent lack of well crystalline phyllosilicates in the lithology. We tentatively conclude that the lithology has been heated dehydrating the hydrous phases. However, this lithology deserves further exploration by TEM work.

### C1/2 Lithology

The C1/2 fragment present in polished thin section PL19149 was classified mainly based on petrographic texture, the high abundance of matrix, and the high degree of aqueous alteration of matrix components and chondrules. The mean size of relic chondrules (~250 μm) clearly indicates a CM-related heritage as well as the observed types of CAIs (e.g., dominance of spinel-diopside inclusions; MacPherson and Davis 1994). The same is true for the chondrule abundance: The C1/2 lithology has a similar abundance as that obtained by Rubin and Wasson (1986; ~15 vol% versus ~20 vol%, respectively). All the above-mentioned observations are well supported by the oxygen isotope analysis of the C1/2 lithology, which is consistent with being a CM chondrite-related clast.

### C1 Lithology

The C1 lithology in Aguas Zarcas is mineralogically similar to xenolithic C1 clasts in many meteorites, including ordinary chondrites, ureilites, and HEDs (e.g., Brearley and Prinz 1992; Zolensky et al. 1996; Patzek et al. 2018a; Chan et al. 2018; Goodrich et al. 2019; Kebukawa et al. 2019), but different to the ungrouped C1 chondrite Flensburg (Bischoff et al. 2021). The

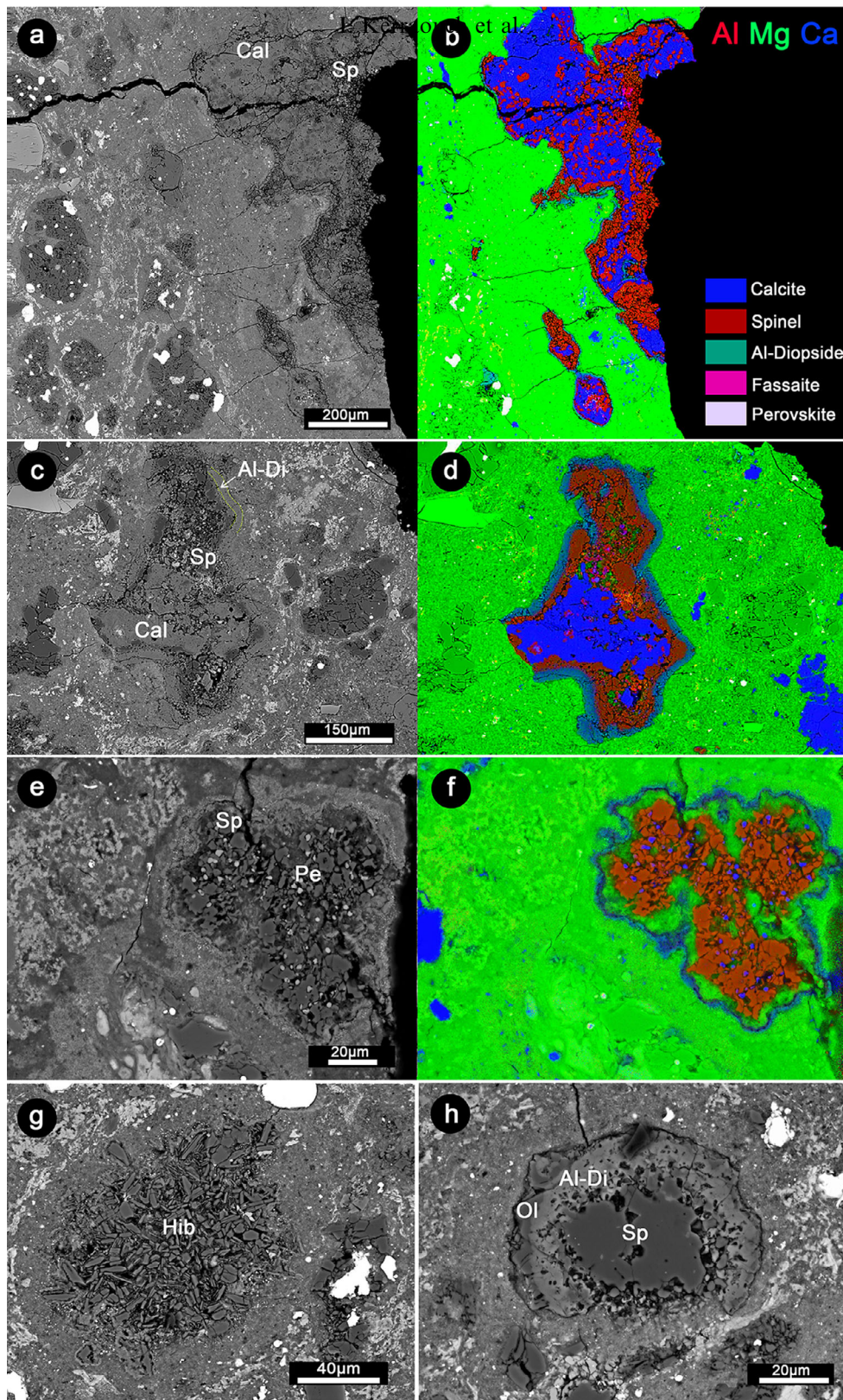


Fig. 15. Backscattered electron images of different types of CAIs within Met-1. a, b) Calcite-rich, spinel-bearing CAIs. c, d) Another calcite- and spinel-rich CAI; color code in the elemental maps of (b) and (d): Al (red; mainly indicating spinel), Mg (green; typical element within the dust rim and matrix), and Ca (blue; related to calcite). e) Spinel-rich CAI within the C1/2 lithology. f) Elemental map of the spinel-rich CAI of (e) showing a phyllosilicate matrix (green) between the spinel-rich core (red-brown) and the outer rim of Ca pyroxene (bluish). g) CAI mainly consisting of hibonite laths. h) Fragment of a round CAI with a spinel core surrounded by Al-rich diopside and an outer rim of olivine. Sp = spinel, Al-Di = Al-diopside, Hib = hibonite, Cal = calcite, Ol = olivine, Pe = perovskite.



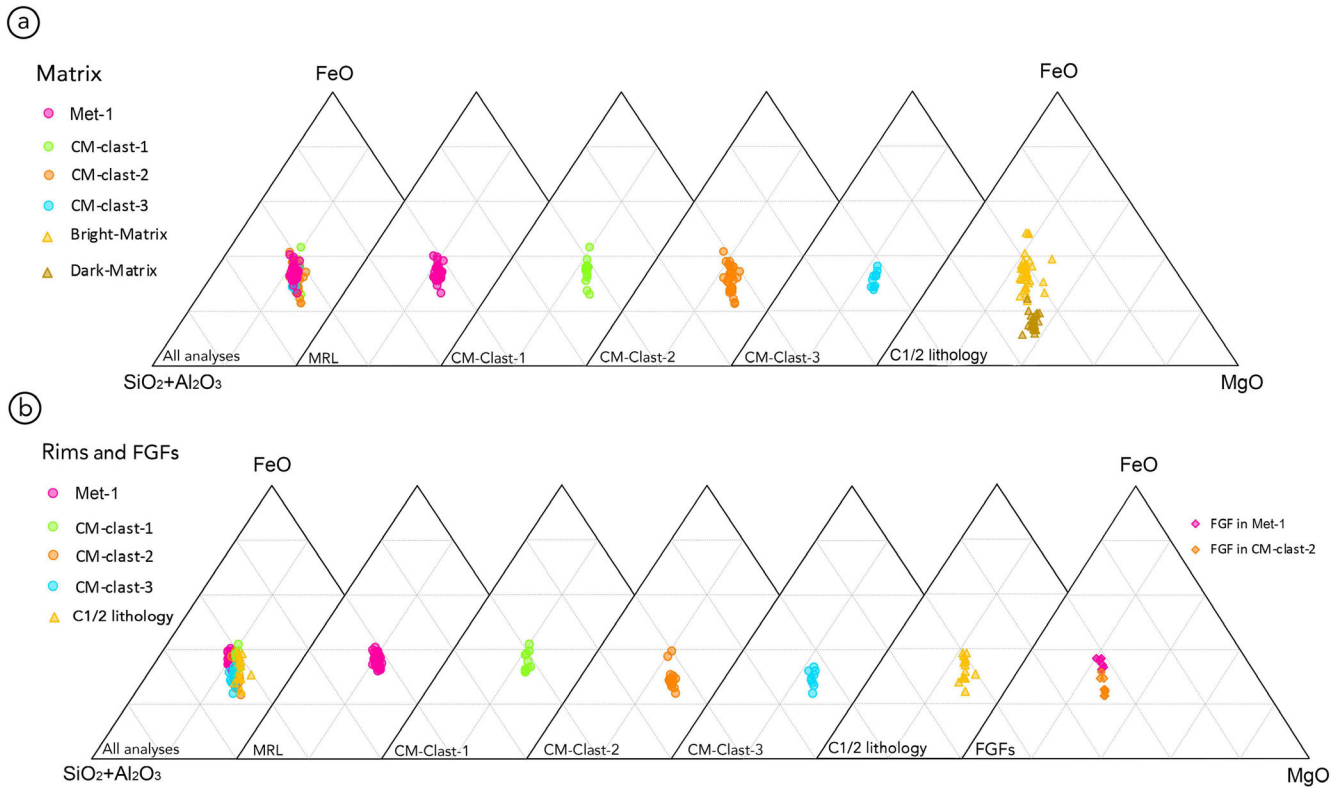


Fig. 16. Ternary FeO-SiO<sub>2</sub> + Al<sub>2</sub>O<sub>3</sub>-MgO diagram (wt%) showing compositional variations of phyllosilicates in the different lithologies of Aguas Zarcas samples: (a) matrix and (b) rims and FGFs.

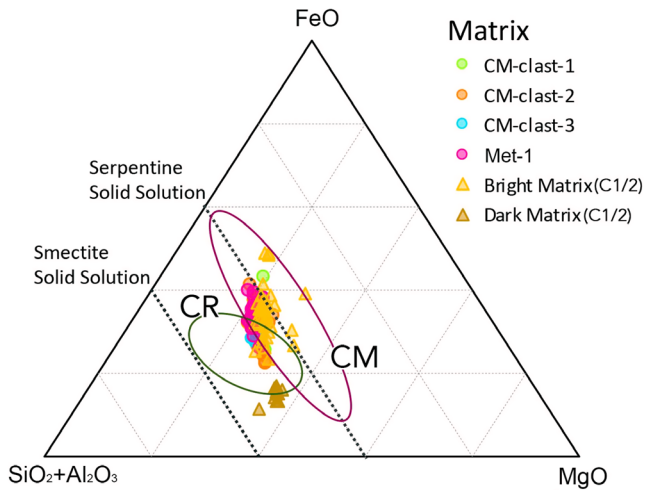


Fig. 17. Ternary FeO-(SiO<sub>2</sub> + Al<sub>2</sub>O<sub>3</sub>)-MgO diagram (wt%) showing compositional variations of matrix analyses of the Met-1 lithology (MRL) compared to those of the matrix of CM and CR chondrites. CM and CR fields are from Zolensky et al. (1993) and Weisberg and Huber (2007). The lines for serpentine and smectite solid solutions are shown for comparison.

phyllosilicate composition in the studied C1 lithology is unlike that of the CM lithologies in Aguas Zarcas (Fig. 24). Thus, it is not clear if it is directly related to

CM chondrites. Only more detailed analyses of larger volumes of the Aguas Zarcas C1 lithology (and O isotope measurements) will reveal potential relationships to other astromaterials.

### Degree of Alteration

Carbonaceous chondrites of types 1 and 2 have altered matrix material composed primarily of cronstedtite and other serpentine phases, tochilinite, carbonates, secondary sulfides, oxides, etc., a clear indication of aqueous alteration (e.g., Zolensky and McSween 1988; Endress and Bischoff 1996; Endress et al. 1996; Alfing et al. 2019; Morlok et al. 2006; DeLeuw et al. 2010; Bischoff et al. 2021). Fe in most type 1 and 2 chondrites is partially to completely oxidized or sulfidized. The CR2 chondrites are in general less altered, retaining more abundant metal (e.g., Bischoff et al. 1993; Weisberg et al. 1993).

Rubin et al. (2007) devised an index to define the degree of CM alteration by tracking metal abundance, alteration of chondrule phenocrysts, and the composition of TCIs. These compositions define their petrologic subtypes ranging from 2.6 (moderately altered) to 2.0 (totally altered). They showed that this sequence is correlated with decreasing S/SiO<sub>2</sub> and

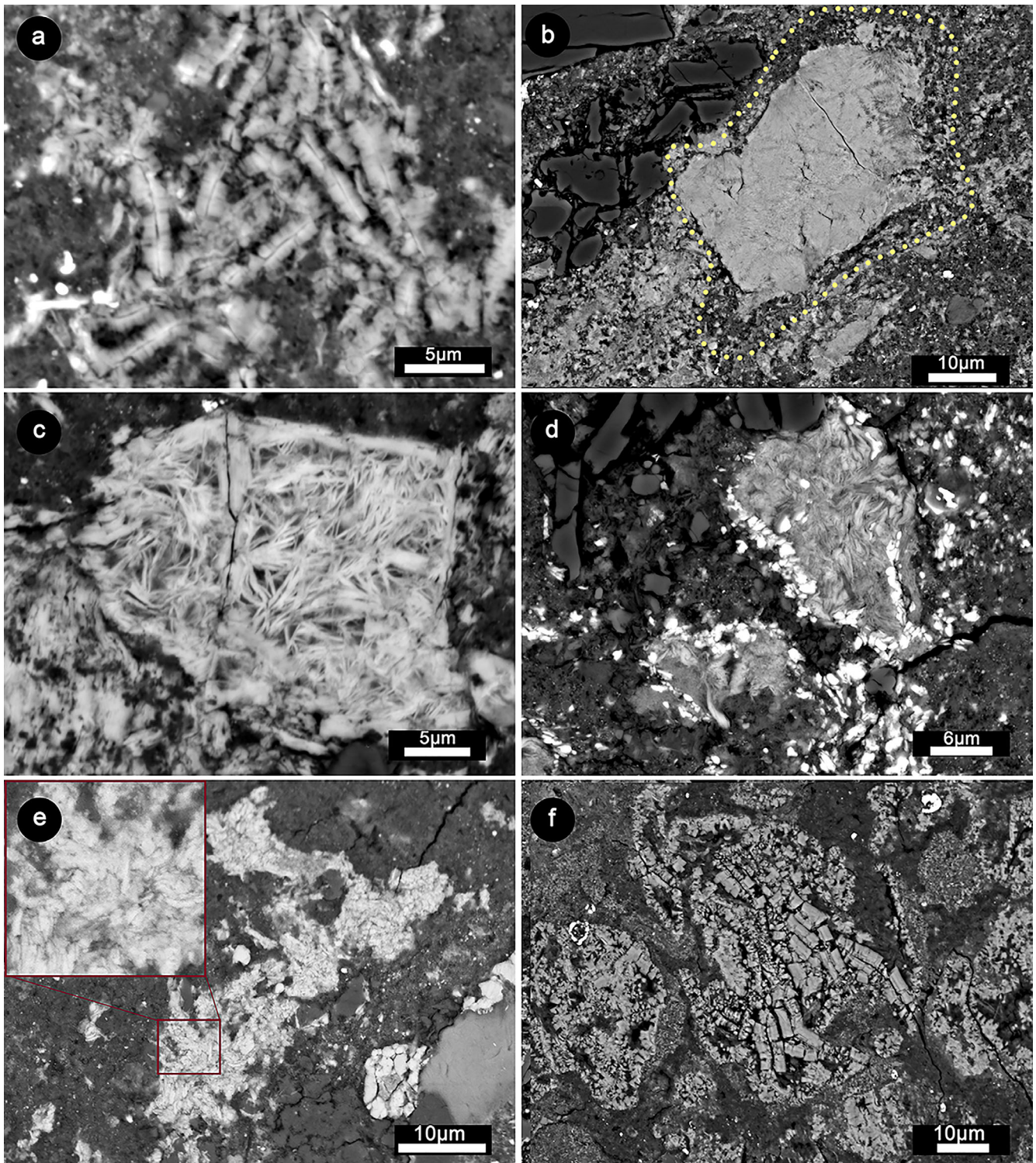


Fig. 18. Backscattered electron images of TCI in the Aguas Zarcas chondrite. a) Fibers of cronstedtite and tochilinite within the Met-1. b) Relatively compact TCI surrounded by a thin rim of accretionary dust within the CM-clast-1. c) Fine-grained TCI with abundant fibers of tochilinite within the CM-clast-2. d) S-rich TCI within the CM-clast-3. e) TCIs within Met-2. f) TCIs (cronstedtite-rich) within a relic chondrule of the C1/2 lithology.



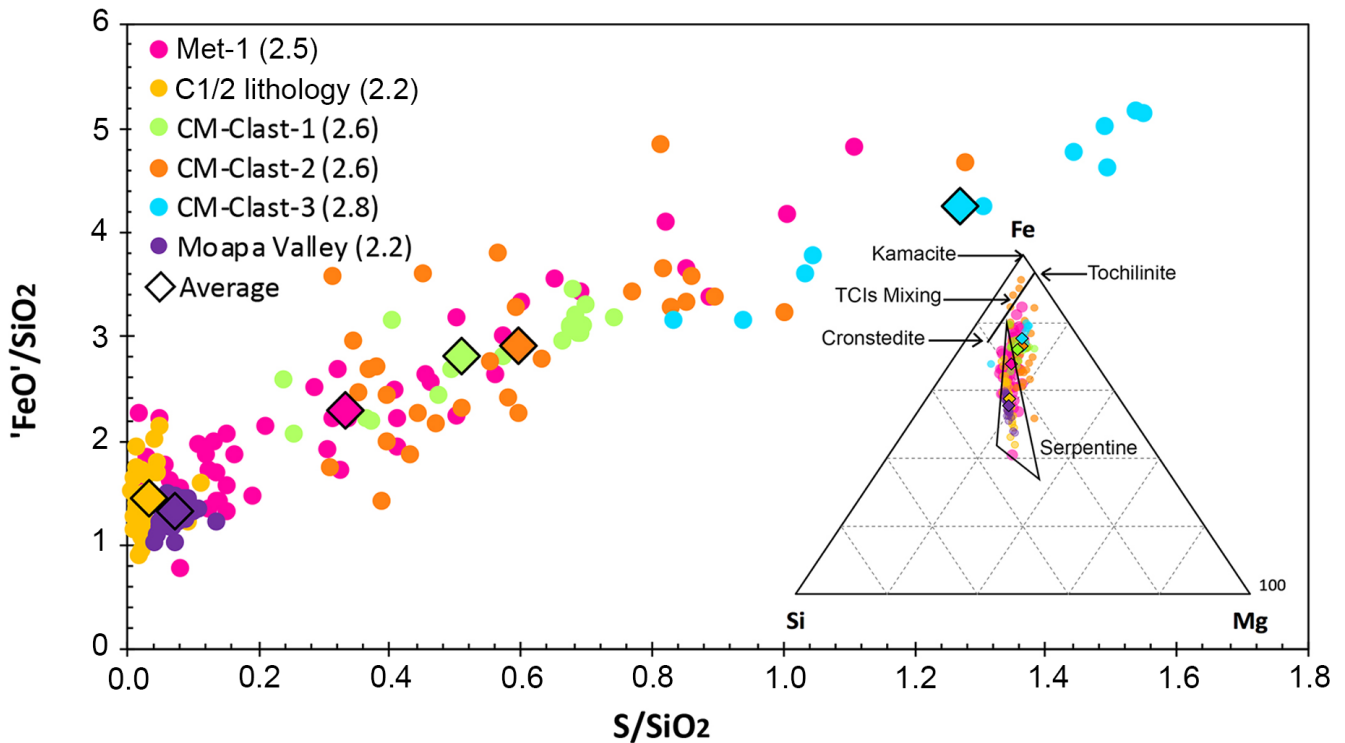


Fig. 19. “FeO”/SiO<sub>2</sub> versus S/SiO<sub>2</sub> ratio for different lithologies in Aguas Zarcas. The C1/2 lithology shows the lowest values indicating the lowest petrologic subtype concerning the degree of aqueous alteration. The ternary SiO<sub>2</sub>-S-FeO diagram (wt%) shows the evolution of S in the TCIs, according to progression of the petrographic type value.

Table 3. Mean concentration of selected elements (in wt%) and element ratios of TCI in different lithologies of Aguas Zarcas.

	Met-1 (n = 48)	CM-Clast-1 (n = 20)	CM-Clast-2 (n = 26)	CM-Clast-3 (n = 10)	C1/2 lithology (n = 14)
SiO <sub>2</sub>	2.1 ± 4.2	16.8 ± 3.1	16.0 ± 2.9	11.8 ± 1.7	26.4 ± 2.1
FeO	42.7 ± 5.7	45.8 ± 3.7	44.9 ± 5.9	40.2 ± 2.9	37.0 ± 5.1
MgO	11.2 ± 2.0	10.3 ± 1.9	11.9 ± 3.4	10.0 ± 0.8	15.3 ± 2.9
S/SiO <sub>2</sub>	0.3 ± 0.3	0.6 ± 0.2	0.6 ± 0.2	2.3 ± 0.3	0.03 ± 0.02
“FeO”/SiO <sub>2</sub>	2.3 ± 0.4	2.8 ± 0.4	2.9 ± 0.8	4.3 ± 0.8	1.5 ± 0.3
Petrologic type	<b>2.5</b>	<b>2.6</b>	<b>2.6</b>	<b>2.8</b>	<b>2.2</b>

“FeO”/ SiO<sub>2</sub> in TCIs. In this study, we also use these chemical relations to define the petrologic subtypes in the different CM fragments of the Aguas Zarcas meteorite. For comparison, as already mentioned above, the CM1 Moapa Valley (King et al. 2017) was studied; this meteorite shows pronounced similarities to the Aguas Zarcas C1/2 lithology.

#### Alteration of Met-1

The abundance of metal in Met-1 indicates a relatively low degree of aqueous alteration. Few metal grains in the matrix or in chondrules show rimming with tochilinite, typically a hallmark of incipient aqueous alteration in CM chondrites

(Tomeoka and Buseck 1985). Using studies of Palmer and Lauretta (2011), this observation corresponds to alteration stage 1 of the aqueous alteration scale 0–4, indicating the beginning of replacement of metal grains by S-rich fluids within a fresh matrix (1). The overall abundance of phyllosilicates, TCIs, and carbonates is high in Met-1, indicating that the lithology has undergone a moderate to high degree of aqueous alteration (2). Thus, the relatively high metal content is unusual. Based on Rubin et al. (2007) and Lentfort et al. (2020), the classification of Met-1 (based on the “FeO”/SiO<sub>2</sub> ratio) is 2.5 (Fig. 19), which is also incompatible with the high abundance of unaltered metal. This may indicate the immature,

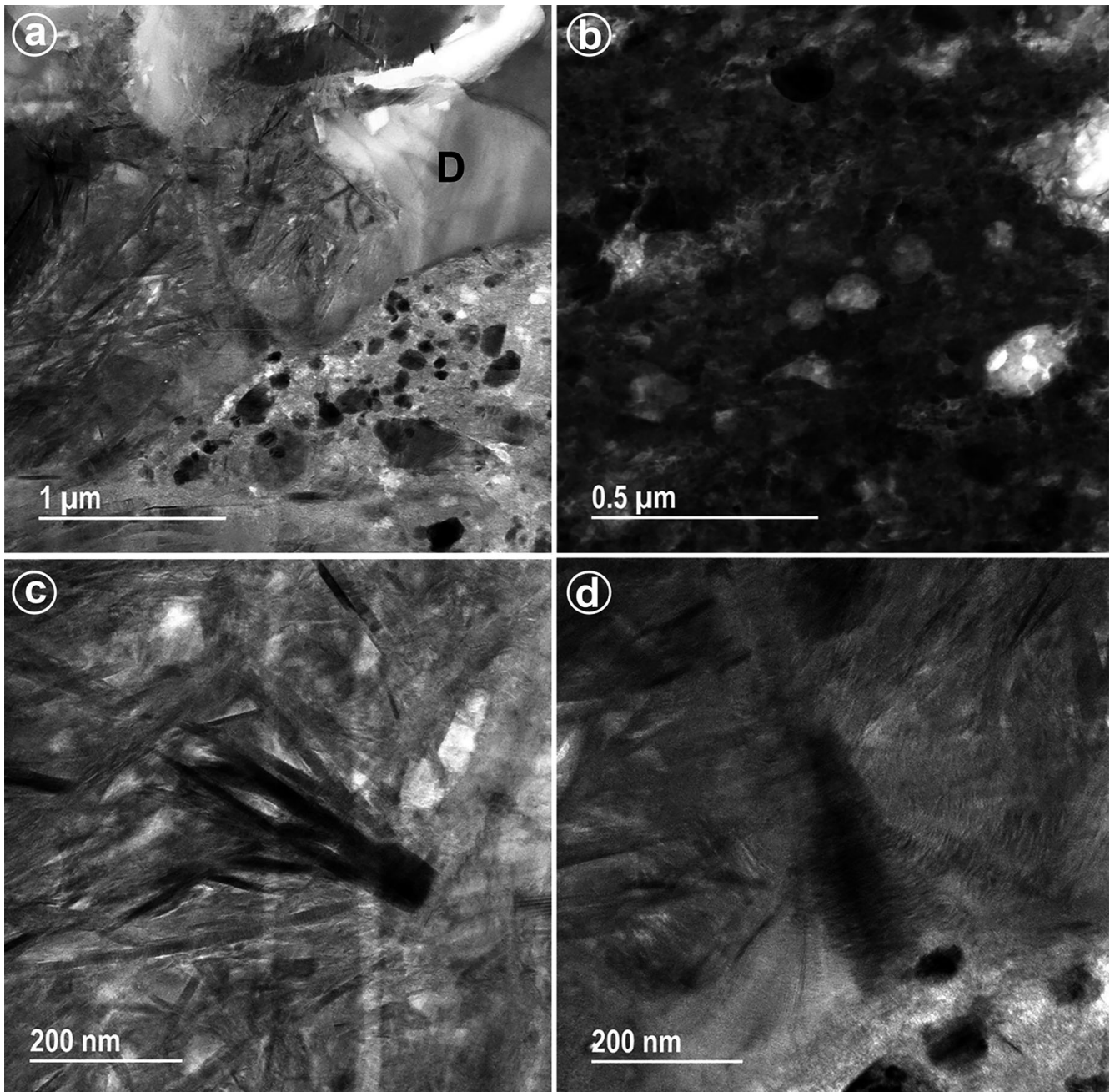


Fig. 20. Bright-field TEM images of matrix in Met-2. None of the “phyllosilicate” phases shows lattice fringes probably indicating heating. a) Lower magnification view of several typical matrix lithologies. The upper left half of the image shows flaky phyllosilicates, the lower right is illustrating spongy material. All black phases are Fe-Ni sulfides, oxides, and Fe carbides. A larger diopside (“D”) grain is present. b) Spongy phyllosilicate material containing Fe-Ni sulfides, oxides, and Fe carbides (all black). c) Large phyllosilicate crystal (compositionally serpentine). d) Possible Povlen (sector) serpentine, although no 0.7 nm fringes were apparent (again probably due to heating).

unequilibrated nature of its aqueous alteration phases (Palmer and Lauretta 2011). However, it is more likely that Met-1 is simply not directly related to CM chondrites, as suggested above. Thus, it is not appropriate to classify this lithology using Rubin

et al.’s CM-derived scale. Additionally, the numerous fractures within the chondrule rims that do not extend into the matrix may indicate post aqueous alteration heating (Hanna et al. 2020). TEM observations are necessary in order to better

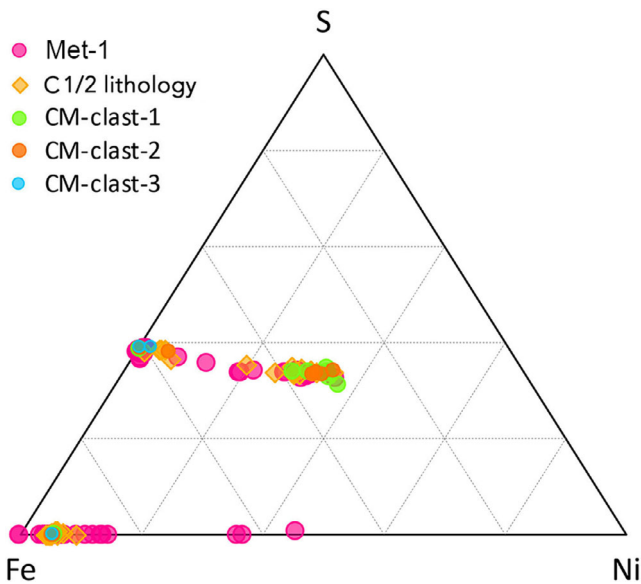


Fig. 21. Fe-Ni-S ternary diagram of metals and sulfides within different lithologies of Aguas Zarcas.

characterize the matrix, and to learn, whether it has been affected by heating.

#### Alteration of Met-2

The Met-2 lithology has twice as much metal and sulfides (5 vol%) compared to Met-1. The matrix is dominated by poorly crystalline phyllosilicate material, which could mean that Met-2 did not really suffer strong aqueous alteration. But, some chondrules show a slight alteration of silicates and the matrix material bears similarity to briefly heated CM chondrites (Tonui et al. 2014). The organics in Met-2 indicate no pronounced heating (Kerraouch et al. 2020), but permit brief heating, as suggested by the TEM observations. Accordingly, Met-2 could be CM-related with a very low degree of aqueous alteration and subsequent heating. Thus, it is apparently unrelated to Met-1.

#### C1/2 Lithology

Evidence of extensive aqueous alteration in the C1/2 lithology includes the formation of serpentine from Fe-rich phases, including cronstedtite, and a lack of tochilinite probably as a result of high peak temperatures and/or higher  $f_{O_2}$  conditions (Zolensky et al. 1997). However, some Fe,Ni-metal grains remain. Only about 3 vol% of the lithology is olivine and pyroxene occurring in some relic chondrules or as clasts in the matrix surrounded by phyllosilicates. According to Rubin et al. (2007), this indicates a CM2.2 subtype classification. Comparing this fragment to the CM1 Moapa Valley, the C1/2 lithology plots in the lowest area of the S/SiO<sub>2</sub>

versus “FeO”/SiO<sub>2</sub> diagram (Fig. 19), even slightly lower than CM1 chondrite Moapa Valley. However, the presence of residual mafic silicates indicates a classification between 1 and 2, in contrast to completely altered CM1s like ALH88045 with no remaining metal or anhydrous silicates (Zolensky et al. 1997).

Additionally, the bulk oxygen isotope data of the C1/2 lithology obtained in this study ( $\delta^{18}O = 10.8$ ;  $\delta^{17}O = 3.2$ ) can probably be more related to the water/rock ratio. As shown by the totally altered CM1 EET 83334 (which is unlike C1/2 lithology, since no olivine is observed; Zolensky et al. 1997), and has a normal O-isotope composition, there is apparently not a direct correlation between bulk O-isotope composition and degree of aqueous alteration. After Clayton and Mayeda (1963), the water–rock ratio also has an important role in determining the final bulk O-isotope composition for CMs.

#### Does a Genetic Correlation between Met-1 and CR Chondrites Exist?

Three different types of metal occur in CR chondrites. These are (1) large spherules and “blobs” in the matrix (sometimes several hundred  $\mu\text{m}$  in size), (2) grains surrounding chondrules (“armored chondrules”), and (3) independent grains inside chondrules (e.g., Bischoff et al. 1993; Weisberg et al. 1993). Very similar observations can be made for Met-1. Large metal blobs exist as shown in Fig. 11 and several chondrules show abundant metal and sulfides at their boundaries with matrix as well as in their interiors (Fig. 13).

A similar statement can be made considering our Ti isotope study of Met-1 (Kerraouch et al. 2020). The Ti isotope composition of the metal-rich lithology (Met-1) of Aguas Zarcas agrees within error with literature values for CR chondrites (Trinquier et al. 2009; Zhang et al. 2012). Concerning O isotopes, Met-1 is certainly richer in <sup>16</sup>O compared to typical CM chondrites, and the  $\Delta^{17}O$  value is lower than that for CR chondrites. However, we cannot completely rule out a genetic relationship with the CR chondrites.

There are significant differences in chondrule sizes in CR chondrites versus those within Met-1 (0.7 mm versus ~0.2 mm, respectively). If the chondrules in the CR chondrites and Met-1 share a common origin, then they must have experienced differential size sorting in the nebula, as has been suggested for other samples of the CR-clan chondrites (e.g., Bischoff 1992; Weisberg et al. 1995).

#### Sulfide–Oxide Aggregate Formation

The polycrystalline, cauliflower-like sulfide–oxide aggregates seen in Met-1 are a common component of



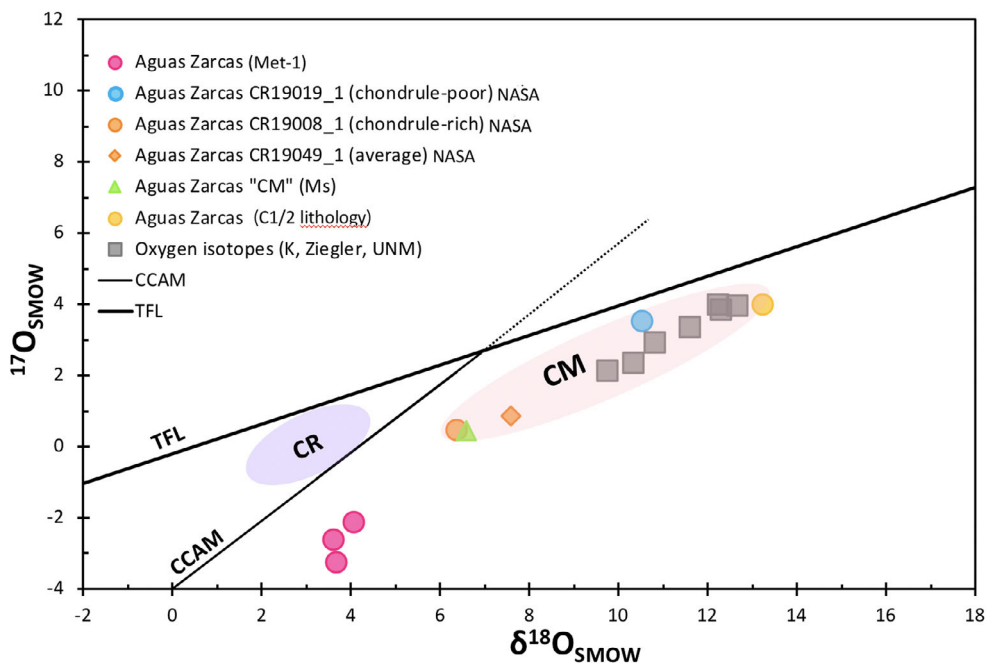


Fig. 22. Oxygen isotope of bulk compositions of different lithologies of Aguas Zarcas. Met-1 and C1/2 lithology (from IfP; Institut für Planetologie) compared to other CM lithologies found in Aguas Zarcas (from IfP and NASA-JSC) from this study and from K. Ziegler (UNM; Meteorite Bulletin Database). CCAM = carbonaceous chondrite anhydrous mineral line; TFL = terrestrial fractionation line.

Table 4. The oxygen isotope compositions of different fragments of Aguas Zarcas.

Sample	$\delta^{18}\text{O}$	$\delta^{17}\text{O}$
Aguas Zarcas "Metal-rich lithology (Met-1)"1	3.6	-2.6
Aguas Zarcas "Metal-rich lithology (Met-1)"2	4.1	-2.1
Aguas Zarcas "Metal-rich lithology (Met-1)"3	3.7	-3.3
Aguas Zarcas "CM" (IfP)	6.6	0.5
Aguas Zarcas CR19008_1 (chondrule-rich)	6.4	0.5
Aguas Zarcas CR19019_1 (chondrule-poor)	10.6	3.5
Aguas Zarcas (C1/2 lithology)	10.8	3.2

IfP = Institut für Planetologie.

CM/CO-like chondrites with low degrees of aqueous alteration, such as Yamato 791198, Queen Alexandra Range 97990, and Acfer 094 (Harries and Langenhorst 2013; Harries and Barth 2017). Mineralogical constraints from Acfer 094, which was first considered to be the first CM3 chondrite (Bischoff and Geiger 1994), suggest that these aggregates might have formed by gas-solid interactions in the nebula at temperatures between 400 and 550 °C (Barth et al. 2018). Observations from more intensely altered CM chondrites indicate that primary pyrrhotite is not stable at the conditions of aqueous alteration experienced by such lithologies (Singerling and Brearley 2020; Lauretta 2005). The pristine state of many massive sulfide grains (Figs. 12a–c) indicates that these are pre-accretionary

high-temperature products that underwent little or no alteration. Sulfide–oxide rims on metal grains next to pristine metal grains (Fig. 25) and polycrystalline sulfide rims below the fined-grained rims of chondrules (Fig. 13c) suggest that these features formed primarily in the nebula. Some of them might have lost pyrrhotite by aqueous alteration, such that pentlandite remained as a dominant phase (Fig. 12f). The presence of the relatively fragile polycrystalline sulfide–oxide aggregates might indicate that Met-1 is a primitive and primary accretionary rock (Metzler et al. 1992) that indeed underwent little post-accretionary processing by aqueous fluids. However, as we discuss below, several inconsistencies remain.

### Origin and Formation of the Aguas Zarcas Parent Body

Unique meteorites, xenolithic clasts, and dark inclusions in brecciated meteorites (e.g., Zolensky and Ivanov 2003; Bischoff et al. 2006, 2018, 2021; Horstmann and Bischoff 2014; Patzek et al. 2018a, 2018b; Kerraouch et al. 2018, 2019a, 2019b; Ebert et al. 2019a; Lentfort et al. 2020) remind us that there is a much wider range of primitive materials than is currently represented by known meteorites. These unusual samples provide new information about the early solar system, reveal previously unknown parent bodies, and help to unravel the different processes of

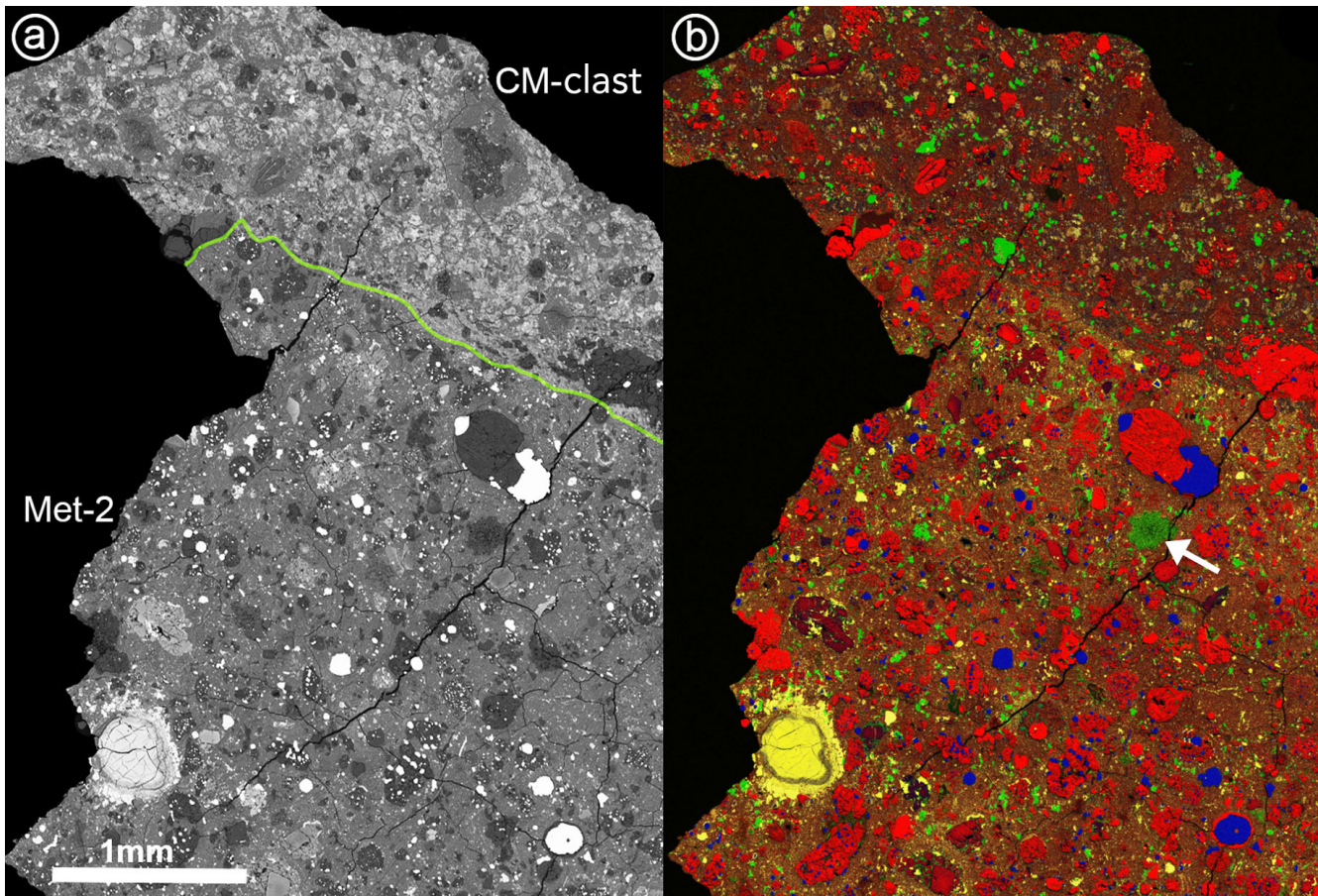


Fig. 23. a) BSE image of metal-rich lithology MET-2 (lower part) in JSC Mount 3, and (b) matching element map of same area. Mg is red, Ca is green, Fe is blue, and S is yellow. There is a much higher abundance of metals and sulfides in MET-2 than in adjacent CM material (upper part), but aside from this, these two lithologies appear to be very similar with respect to the size and abundance of chondrules. Arrow in (b) points to a fine-grained object that is a plagioclase-rich CAI.

their formation. The Aguas Zarcas fall was very generous and delivered a wide variety of carbonaceous chondrite lithologies. Some of these are familiar CM lithologies, but others are unique and unusual (such as Met-1, Met-2, and C1/2 lithology in this study), which allow us to dig into the history of their formation. Aguas Zarcas is complex breccia at all scales.

Considering the high abundance and the intensity of mixing of different lithologies within Aguas Zarcas, impact processes played a very important role in the formation history of the Aguas Zarcas parent body. The mineralogy of the individual fragments suggests that the characteristic signatures of aqueous alteration are still visible and have not been significantly modified during brecciation and re-accretion. Anyway, if we consider that the agglomeration of the brecciated Aguas Zarcas parent body occurred by a collisional compaction (e.g., Blum and Schröpler 2006), the important question related to required impact processes

is: Do we still recognize effects of these collisions within the different lithologies of the Aguas Zarcas? Here, we propose the following scenario, which explains the mixing mechanisms during formation of this breccia.

According to our studies of the five different lithologies of this unique fall, Aguas Zarcas has experienced a complicated history, since the formation of its first particles (the most primitive material), experiencing a wide range of processes, such as aqueous alteration and impact brecciations, until the re-accretion and formation of the final parent body, from which the meteorite was ejected. The possible proposed scenario can be summed up in four main stages: The first stage is linked to the formation of the different CM chondrite lithologies, while the second stage is related to an impact with another (CR-related) body and fragmentation of both bodies. The third stage comprises the formation of the Aguas Zarcas parent body by re-accretion, which involves the formation of the metal-rich lithologies and probably other lithologies within it. After

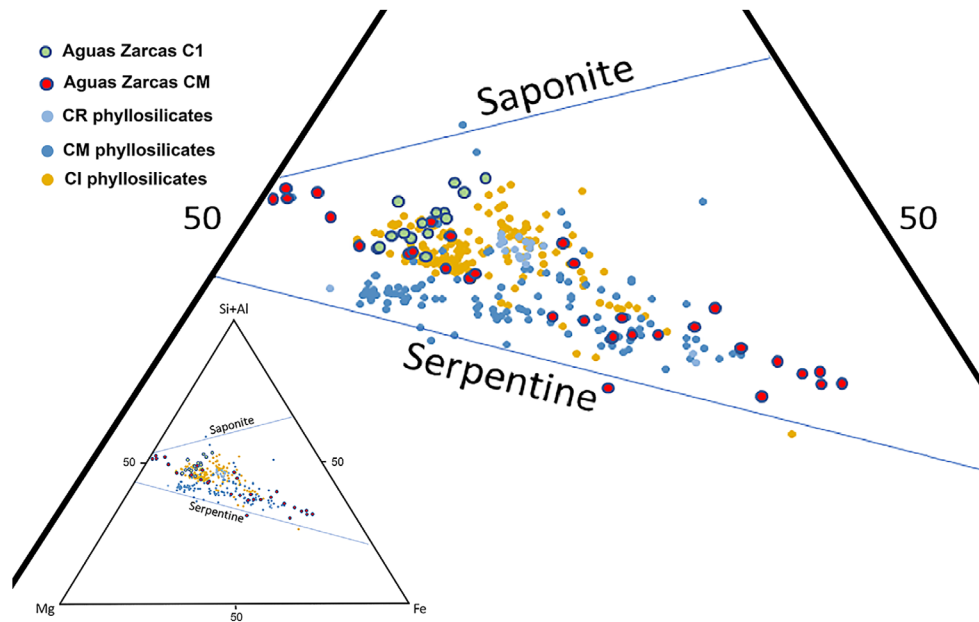


Fig. 24. Composition of Aguas Zarcas C1 and CM phyllosilicates displayed on an atom% ternary with Si + Al, Mg, and Fe vertices. Compositional ranges of phyllosilicates from eight CM (and Essebi), three CR, and two CI chondrites are shown for comparison (from Goodrich et al. 2019). Lines indicate the actual range of compositions of terrestrial serpentines and saponite.

the final formation of the brecciated parent body of Aguas Zarcas, another impact on the asteroid (Stage 4) led to fragmentation of the latter basically triggering the ejection of some of its fragments to Earth. The diagram in Fig. 26 summarizes the four stages and will be discussed in detail below.

#### *Stage 1: Formation of a Very Primitive CM Parent Body*

The abundance of CM-related chondrite material (like CM-clasts, C1/2 lithology, and C1 lithology) in Aguas Zarcas may indicate that the whole scenario took place in a CM chondrite formation region. It is very likely that all these lithologies (CM and CM-related chondrites) were formed in a single very primitive parent body of small size (Fig. 26, Stage 1), and which underwent large-scale alteration that affected the parent body at multiple times and locations (depending on depth and fluid distribution). These processes interacted with primary phases to form the secondary minerals and result in the formation of a parent body having lithologies of the different petrographic subtypes (CM2.8, CM2.6, CM1/2, etc.).

#### *Stage 2: Impact by a Possibly CR-Like Asteroid and Fragmentation*

The XCT data of the JSC.40 and JSC.06 fragments in this study show that the Aguas Zarcas fragments represent some lithologies, which are very rich in metal (Fig. 1;

Fig. S1). The MS-2 and CR19.01 fragments are represented by two different metal-rich lithologies as their main lithology (Met-1 and Met-2, respectively), these perceptions are more clear in the investigated sections PL19125, PL19111, and JSC-Mt1 (Figs. 3a, 3b, and 4a). However, the Ti-isotope measurements of the Met-1 lithology (Kerraouch et al. 2020) suggest a close relationship with the CR-chondrite group. These observations suggest that the first primitive CM parent body was probably impacted by a CR-related parent body.

Since we do not observe clearly shock-related feature or evidence of lineation produced by preferential propagation of shock waves (e.g., Trigo-Rodríguez et al. 2006; Trigo-Rodríguez and Blum 2009), we propose that the impact of the CR-related body into the CM parent body was of rather low energy. This CR-related parent body is probably the main source of metal and chondrules that are surrounded by metal (similar to those in CR chondrites) in these metal-rich lithologies in Aguas Zarcas (Fig. 26, Stage 2). Due to this impact, the two parent bodies (CM and CR) were possibly catastrophically destroyed resulting in a mixture of different components from the CM target and CR-like impactor in the form of a “dusty and rocky cloud,” which contains dust, larger objects (e.g., chondrules, CAIs, etc.), and also fragments of well-consolidated rock (e.g., well-preserved and lithified rock fragments of CM-type). All these different components may be described as objects of three categories:



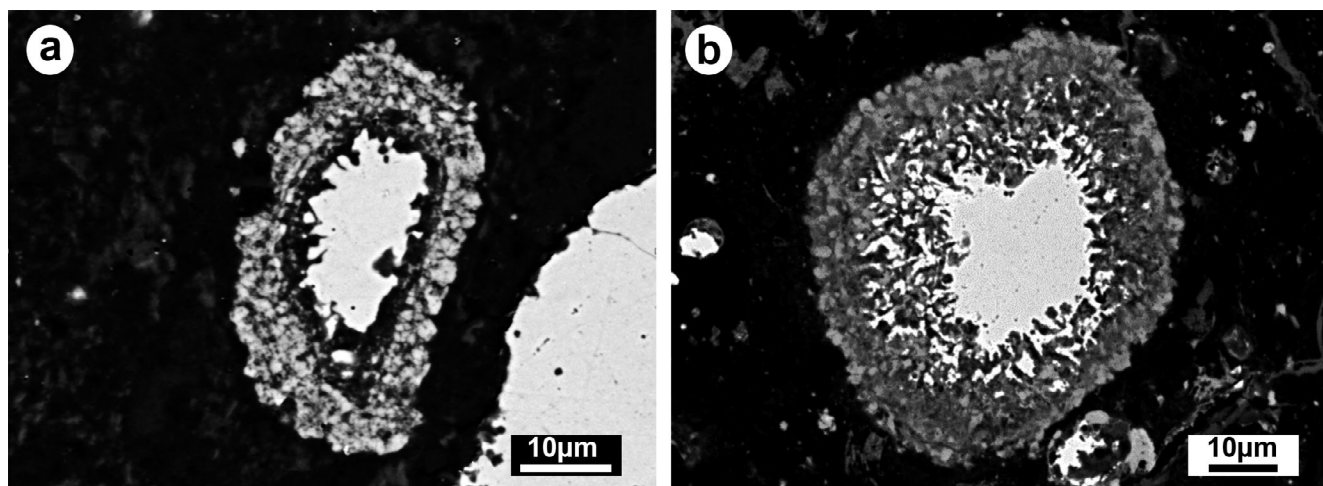


Fig. 25. SEM-BSE images of selected sulfide–oxide aggregates in Met-1 within the Aguas Zarcas (a) and in Acfer 094 (PL93040; b). Metal is abundant in the central parts. Light gray phases are sulfides and darker gray phases are oxides.

1. Category 1: Objects of macroscopic size from the original parent bodies (boulders, pebbles, fragments of different CM subtypes, C1/2, etc.) that are well lithified.
2. Category 2: Objects of millimeter- to microscopic-sized components of CM- and CR-type materials. (e.g., chondrules, CAIs, silicate grains, metal and sulfide grains, etc.).
3. Category 3: Objects that can be best described as fine-grained microscopic “dust” of different components (e.g., TCIs, phyllosilicates; see legend of Fig. 26).

All of these components from different categories are available for re-accretion into a new parent body and form new lithologies simultaneously.

### *Stage 3: Re-accretion and Formation of the Metal-Rich Lithologies within the AZ Parent Body*

The observations made on the Met-1 lithology, that is, the coexistence of unaltered metal and highly altered phyllosilicates, indicate a disequilibrium between the different phases. This might imply that the components are genetically not related, but rather derive from different parent bodies. Additionally, most chondrules are texturally similar to those of CR chondrites (Fig. 13d), but silicates and phyllosilicates are more characteristic for CM chondrites. The presence of intact metal grains and very primitive components such as sulfide–oxide aggregates (Fig. 25a), which probably formed in the nebula (see the Sulfide-Oxide Aggregate Formation section), exhibit a very low degree of aqueous alteration. These unaltered components are strangely surrounded by TCIs, which characterize a petrologic subtype of 2.5 indicating a moderate

alteration. The complex CAIs with abundant Ca-carbonate (Figs. 15a–d) also indicate strong alteration.

Comparing all these components, some show a strong degree of alteration and others are less altered or even unaltered. Therefore, all these observations indicate that the Met-1 is a microbrecciated lithology, whose components have probably formed in different environments, possibly within the CR- and CM-type parent bodies. The chemical data support this idea.

Therefore, we suggest that this unusual metal-rich lithology Met-1 (and maybe also Met-2) was possibly formed by mixing components of category 2 (e.g., metals, chondrules, CAIs) and category 3 (dust: TCIs and phyllosilicates) followed by compaction. Simultaneously, fragments of the CM parent body (i.e., category 1 objects) are available and accrete together with the newly formed metal-rich lithologies to form the final brecciated parent body of Aguas Zarcas (Fig. 26, Stage 3).

### *Stage 4: The Final Aguas Zarcas Parent Body*

After re-accretion and consolidation of the final parent body, it was struck by another asteroid leading to the ejection of material that is finally traversing to Earth leading to the fall of the Aguas Zarcas meteorite on April 19, 2019 in Costa Rica.

Additionally, some Aguas Zarcas lithologies (like Met-2) show evidence of being modified by a brief heating event. This heating period is not necessarily linked to an early event during its evolution prior to brecciation, but rather may be related to the later impact compaction. Jutzi and Michel (2020) show that the effects of compaction are very similar to those of heating. These authors state that during impact escaping

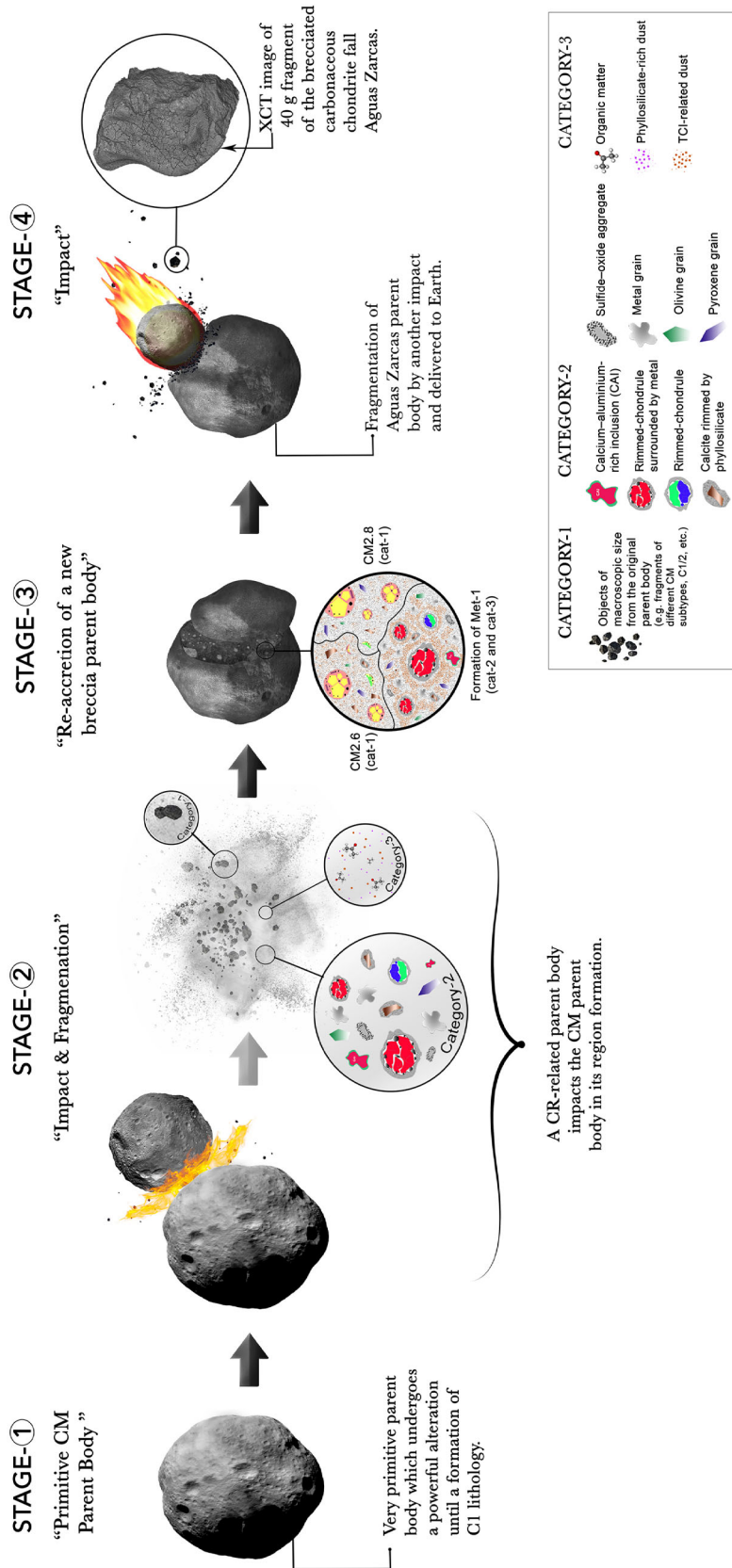


Fig. 26. Schematic portrayal of the history of the formation of the Aguas Zarcas parent body. Stage 1: Formation of primitive CM parent body. Stage 2: Impact of the primitive CM parent body with a CR-related parent body and fragmentation of both bodies; three categories of impact-related components result from this process (a) at the macroscopic scale (category 1): boulders and pebbles; (b) at the microscopic scale (category 2): chondrite components like chondrules and CAIs; and (c) with a very small grain size (category 3): dust of phyllosilicates and TCIs. The three circles show the objects from categories 1, 2, and 3 (e.g., CM clasts, chondrules, TCIs, metal grains) after the collision of the CM and CR-type parent bodies. Stage 3: Aguas Zarcas breccia in its final state: Re-accretion and formation of the Aguas Zarcas parent body including the formation of Met-1 (-2) lithologies. As an example, the circle should illustrate the coexistence of the Met-1 lithology with two types of CM-clasts (CM2.6 and CM2.8). Stage 4: The polymict Aguas Zarcas parent body was impacted by another asteroid in order to deliver fragment(s) to Earth. The circle shows a CT image of the brecciated carbonaceous chondrite.

material experiences a relatively high degree of compaction, which is independent of the impact energy. The compaction of the bound target material increases with increasing impact energy; however, this increase is much less significant than that of the escaping rock material.

Other small clasts in Aguas Zarcas, which are distinct from CM chondrites (e.g., the sub-mm-sized clasts of the C1 lithology), could be incorporated into the Aguas Zarcas parent body as small projectiles during the later evolution of the parent body surface materials or were part of the CR-related impactor (Trigo-Rodríguez 2015; Chesley et al. 2020). It is well known that the CR chondrites contain C1-type objects, the so-called dark inclusions (e.g., Endress et al. 1992, 1994; Patzek et al. 2018a, 2018b).

### **Aguas Zarcas Shows Similarities to the Surface of Asteroids Ryugu and Bennu**

The rapid recovery of the Aguas Zarcas meteorite after its fall provides an opportunity to investigate a freshly fallen, relatively uncontaminated and highly brecciated meteorite for comparison to the samples to be returned from C-group asteroids by the Hayabusa2 (JAXA) and OSIRIS-REx (NASA) spacecraft. Hayabusa2 will return samples from asteroid Ryugu (162173), a C-type asteroid, on December 6, 2020 while OSIRIS-REx will return samples from asteroid Bennu (101955), a B-type asteroid, in September 2023.

Spectroscopic observations of Ryugu compared to laboratory measurements of meteorites suggest that Ryugu is most similar to heated CI and heated CM chondrites, although neither material shows an exact match (Matsuoka et al. 2015; Kitazato et al. 2019). In contrast, spectroscopic observations of Bennu indicate that it is most consistent with CM chondrites, although a relationship to heated CM (Hanna et al. 2019) or CI chondrites (e.g., Hamilton et al. 2019) is also possible. Both asteroids are regarded to consist of materials altered by aqueous alteration (e.g., Hamilton et al. 2019; Watanabe et al. 2019). Nevertheless, Ryugu could contain stronger heated lithologies than Bennu, resulting in different hydration levels between the two asteroids (Michel et al. 2020; Sugita et al. 2019).

However, a recent numerical simulation study by Michel et al. (2020) suggests that Bennu and Ryugu could have been born from the destruction of the same asteroid although their hydration levels are different. During large asteroid destruction events in the asteroid belt, fragments escape and then re-agglomerate to form aggregates, some of which have the shape of a spinning top. To explain the different hydration levels of the two bodies, the paper explores two possible explanations

based on the team's computer simulations. The first explanation is that the material of the two asteroids would experience different levels of both heating and compaction at parent-body impact. Thus, they would have different macroporosity to achieve the same bulk density. In this case, Bennu formed from material closer to the original surface, when the parent asteroid was disrupted, while Ryugu contained more material from near the parent body's original center. The second explanation is that the two asteroids would have undergone a different level of heating, but a similar level of compaction during the disruption. If this is the case, Ryugu would have been sourced from near the impact point, where material can experience high heating, but little compaction. Bennu's material would have come from a region that did not undergo as much heating, and was likely located at a larger distance from the point of impact. Thus, both materials could have the same microporosity, but a different level of hydration.

However, in both cases, we can deduce that the two parent bodies are brecciated asteroids (McCoy et al. 2019). Comparing these observations with our results of the study of different lithologies from the Aguas Zarcas parent body, we notice the presence of different clasts of CM chondrite subtypes in Aguas Zarcas. The difference in degree of aqueous alteration may be due to the different shock intensities experienced in the same parent asteroid (Rubin 2012). The presence of unique and rare lithologies in Aguas Zarcas that are distinct from typical CM chondrite lithologies, indicates a complex mixing of various materials in a highly dynamic environment. During this process, material from various sources was involved that all demonstrate compelling evidence of earlier brecciation. The mixing could have taken place at shallow crustal levels of an asteroid during impacts of foreign bodies (e.g., Lindgren et al. 2013). However, all these aspects may also indicate that the Aguas Zarcas parent body is a transitional asteroid (Trigo-Rodríguez 2015; Trigo-Rodríguez et al. 2019; Lauretta et al. 2019b; Chesley et al. 2020; Michel et al. 2020). This may also suggest that the surfaces of the Bennu and Ryugu asteroids likely host a mixture of hydrated and dehydrated phases (Lauretta et al. 2019a, 2019b; Michel et al. 2020), at least on a small scale (as inclusions), and that the different lithologies of the fresh Aguas Zarcas breccia, which represent different levels of hydration and heating, are good analogs for the types of materials that will be returned from asteroids Bennu and Ryugu.

Short period comets and C-type asteroids could have been exposed to a large flow of impactors of very different nature. As a result, the surface of fragile bodies could end in complex breccias. Aguas Zarcas



may represent a very good example considering the aspects discussed above as given by the variety of carbonaceous lithologies introduced in this paper. However, a recent study by Tanbakouei et al. (2020) shows that the brecciated nature of ungrouped carbonaceous chondrites can be considered to be a possible way to explain the reflectance properties of periodic comets such as, for example, 2P/Encke.

## CONCLUSION

We found that Aguas Zarcas is a complex breccia consisting of various different lithologies as supported by other studies on different fragments of this meteorite (e.g., Davidson et al. 2020; Kebukawa et al. 2020; Kerraouch et al. 2020). We have identified five main lithologies, two of which are new primitive carbonaceous chondrite lithologies never seen before. These are described as metal-rich lithologies (Met-1 and Met-2). (1) The Met-1 is uniquely primitive carbonaceous chondrite material, which shows petrographic characteristics indicating similarities with components in CM and CR chondrite groups. However, the chondrule size and abundance data are clearly different from both and the oxygen isotopes show that this lithology is neither related to CM nor to CR chondrites. The Ti isotopes might suggest a relationship to the CR chondrites, although variations are strongly dependent and explainable by the abundance of CAIs in the sample. This lithology could, therefore, have been formed following an impact between early CM and CR-related parent bodies. (2) The Met-2 is the second metal-rich lithology which is distinct from Met-1 and more related to CM group chondrite lithologies. (3) The third lithology is a C1/2 lithology and probably related to CM chondrites. Its oxygen isotopic composition lies at the upper end of the field for CM group chondrites suggesting that some aqueous alteration may have occurred earlier in its history. (4) A brecciated CM lithology with clasts of different petrologic subtypes. (5) The last one is a C1 lithology. It is not clear yet if it is directly related to CM chondrite lithologies because the phyllosilicate composition is distinct from that of CM lithologies. Mineralogically, it is similar to xenolithic C1 clasts in many meteorite breccias.

The chondrule-poor lithology described in the Meteoritical Bulletin may be related to the CM lithologies discussed in this work, while the chondrule-rich lithology could be similar to one of the metal-rich lithologies discussed here, although the chondrule abundances given in the Meteoritical Bulletin are different to those presented in this work.

In summary, the investigated samples of the Aguas Zarcas breccia show that each sample has been affected

by different processes (e.g., aqueous alteration, heating). The Aguas Zarcas breccia formed by re-accretion of newly formed Met-rich lithologies and CM-lithologies of different degree of aqueous alteration. The samples may be petrologically similar to materials that will be encountered by the Hayabusa2 and OSIRIS-REx sample return missions to near-Earth asteroids Ryugu and Bennu, respectively.

*Acknowledgments*—We thank Ulla Heitmann for sample preparation, Jasper Berndt-Gerdes and Beate Schmitte for analytical assistance, and Josep Trigo-Rodríguez for his constructive review. This work is partly funded by the Deutsche Forschungsgemeinschaft (DFG, German Research Foundation)—Project-ID 263649064—TRR 170 (subproject B05; AB); this is TRR170 Publication No. 122. MZ was also supported by NASA's Emerging Worlds and Hayabusa2 Participating Scientist Programs, and RDH by the OSIRIS-REx Participating Scientist Program (grant 80NSSC18K0229). We thank Robert Ward for the loan of some meteorite samples. The UTCT facility is partially supported by NSF grant EAR-1762458. We thank Dr. Matthew Colbert for collection of the XRCT data of the Aguas Zarcas samples. Mike Weisberg provided useful discussion of our results. This work was also supported in part by the Japan Society for the Promotion of Science KAKENHI (grant numbers JP17H06458 and JP19H05073 to YK). Open Access funding enabled and organized by ProjektDEAL.

*Editorial Handling*—Dr. Josep M. Trigo-Rodríguez

## REFERENCES

- Alfing J., Patzek M., and Bischoff A. 2019. Modal abundances of coarse-grained (>5  $\mu\text{m}$ ) components within CI-chondrites and their individual clasts—Mixing of various lithologies on the CI parent body(ies). *Geochemistry—Chemie der Erde* 79:125532.
- Barth M. I. F., Harries D., Langenhorst F., and Hoppe P. 2018. Sulfide–oxide assemblages in Acfer 094—Clues to nebular metal–gas interactions. *Meteoritics & Planetary Science* 53:187–203.
- Bischoff A. 1992. ALH 85085, Acfer 182, and Renazzo-type chondrites—Similarities and differences. *Meteoritics* 27:203–204.
- Bischoff A. and Geiger T. 1994. The unique carbonaceous chondrite Acfer 094: The first CM3 chondrite (?). *Lunar and Planetary Science* 25:115–116.
- Bischoff A., Palme H., Ash R. D., Clayton R. N., Schultz L., Herpers U., Stöffler D., Grady M. M., Pillinger C. T., Spettel B., Weber H., Grund T., Endreß M., and Weber D. 1993. Paired Renazzo-type (CR) carbonaceous chondrites from the Sahara. *Geochimica et Cosmochimica Acta* 57:1587–1604.
- Bischoff A., Scott E. R. D., Metzler K., and Goodrich C. A. 2006. Nature and origins of meteoritic breccias. In

- Meteorites and the early solar system II*, edited by Lauretta D. S. and McSween H. Y. Jr. Tucson, Arizona: The University of Arizona Press. pp. 679–712.
- Bischoff A., Ebert S., Metzler K., and Lentfort S. 2017. Breccia classification of CM chondrites (abstract #6089). *Meteoritics & Planetary Science* 52:A26.
- Bischoff A., Schleiting M., Wieler R., and Patzek M. 2018. Brecciation among 2280 ordinary chondrites—Constraints on the evolution of their parent bodies. *Geochimica et Cosmochimica Acta* 238:516–541.
- Bischoff A., Alexander C. M. O'D., Barrat J.-A., Burkhardt C., Busemann H., Degering D., Di Rocco T., Fischer M., Fockenberg T., Foustoukos D. I., Gattacceca J., Godinho J. R. A., Harries D., Heinlein D., Hellmann J. L., Hertkorn N., Holm A., Jull A. J. T., Kerraouch I., King A. J., Kleine T., Koll D., Lachner J., Ludwig T., Merchel S., Mertens C. A. K., Morino P., Neumann W., Pack A., Patzek M., Pavetich S., Reitze M. P., Rüfenacht M., Rugel G., Schmidt C., Schmitt-Kopplin P., Schönbächler M., Trieloff M., Wallner A., Wimmer K., and Wölfer E. 2021. The old, unique C1 chondrite Flensburg—Insight into the first processes of aqueous alteration, brecciation, and the diversity of water-bearing parent bodies and lithologies. *Geochimica et Cosmochimica Acta* 293:142–186.
- Blum J. and Schräpler R. 2006. The physics of protoplanetary dust agglomerates. I. Mechanical properties and relations to primitive bodies in the solar system. *Astrophysical Journal* 652:1768–1781.
- Brearley A. and Prinz M. 1992. CI chondrite-like clasts in the Nilpena polymict ureilite: Implications for aqueous alteration processes in CI chondrites. *Geochimica et Cosmochimica Acta* 56:1373–1386.
- Chan Q., Zolensky M., Kebukawa Y., Franchi I., Wright I., Zhao I., Rahman Z., and Utas J. 2018. Primitive oxygen-, nitrogen-, and organic-rich vein preserved in a xenolith hosted in the metamorphosed Carancas meteorite (abstract #1191). 49th Lunar and Planetary Science Conference. CD-ROM.
- Chesley S. R., French A. S., Davis A. B., Jacobson R. A., Brozović M., Farnocchia D., Selznick S., Liounis A. J., Hergenrother C. W., Moreau M. C., Pelgrift J., Lessac-Chenen E., Molaro J. L., Park R. S., Rozitis B., Scheeres D. J., Takahashi Y., Vokrouhlický D., Wolner C. W. V., Adam C., Bos B. J., Christensen E. J., Emery J. P., Leonard J. M., McMahon J. W., Nolan M. C., Shelly F. C., and Lauretta D. S. 2020. Trajectory estimation for particles observed in the vicinity of (101955) Bennu. *Journal of Geophysical Research: Planets* 125:e06363.
- Clayton R. N. and Mayeda T. K. 1963. The use of bromine pentafluoride in the extraction of oxygen from oxides and silicates for isotopic analysis. *Geochimica et Cosmochimica Acta* 27:43–52.
- Davidson J., Alexander C. M. O'D., King A. J., Bates H. C., Foustoukos D. I., Schrader D. L., Bullock E. S., Busemann H., Riebe M. E. I., Schönbächler M., and Clay P. 2020. Samples relevant for carbonaceous asteroid sample return: Coordinated studies of CM chondrites Meteorite Hills 00639 and Aguas Zarcas (abstract #2115). 51st Lunar and Planetary Science Conference. CD-ROM.
- De Leuw S., Rubin A. E., and Wasson J. T. 2010. Carbonates in CM chondrites: Complex formational histories and comparison to carbonates in CI chondrites. *Meteoritics & Planetary Science* 45:513–530.
- Ebert S., Patzek M., Lentfort S., and Bischoff A. 2019a. Accretion of differentiated achondritic and aqueously-altered chondritic materials in the early solar system—Significance of an igneous fragment in the CM chondrite NWA 12651. *Meteoritics & Planetary Science* 54:2985–2995.
- Ebert S., Bischoff A., Harries D., Lentfort S., Barrat J.-A., Pack A., Gattacceca J., Visser R., Schmid-Beurmann P., and Kimpel S. 2019b. Northwest Africa 11024—A heated and dehydrated unique carbonaceous (CM) chondrite. *Meteoritics & Planetary Science* 54:328–356.
- Endress M. and Bischoff A. 1996. Carbonates in CI chondrites: Clues to parent body evolution. *Geochimica et Cosmochimica Acta* 60:489–507.
- Endress M., Keil K., and Bischoff A. 1992. Dark clasts in the Acfer 059/El Djouf 001 meteorite (CR) from the Sahara: Implications for their origin. *Meteoritics* 27:218–219.
- Endress M., Keil K., Bischoff A., Spettel B., Clayton R. N., and Mayeda T. K. 1994. Origin of dark clasts in the Acfer 059/El Djouf 001 CR2 chondrite. *Meteoritics* 29:26–40.
- Endress M., Zinner E., and Bischoff A. 1996. Early aqueous activity on primitive meteorite parent bodies: Evidence from <sup>53</sup>Mn. *Nature* 379:701–703.
- Frank D. R., Zolensky E. M., and Le L. 2014. Olivine in terminal particles of Stardust aerogel tracks and analogous grains in chondrite matrix. *Geochimica et Cosmochimica Acta* 142:240–259.
- Goodrich C., Zolensky M., Fioretti A., Shaddad M., Downes H., Hiroi T., Kohl I., Young E., Kita N., Śliwiński M., Hamilton V., Riebe M., Busemann H., Macke R., Ross D., and Jenniskens P. 2019. The first samples from Almahata Sitta showing contacts between ureilitic and chondritic lithologies: Implications for the structure and composition of Asteroid 2008 TC3. *Meteoritics & Planetary Science* 54:2769–2813.
- Hamilton V. E., Simon A. A., Christensen P. R., Reuter D. C., Clark B. E., Barucci M. A., Bowles N. E., Boynton W. V., Brucato J. R., Cloutis E. A., Connolly H. C., Donaldson Hanna K. L., Emery J. P., Enos H. L., Fornasier S., Haberle C. W., Hanna R. D., Howell E. S., Kaplan H. H., Keller L. P., Lantz C., Li J.-Y., Lim L. F., McCoy T. J., Merlin F., Nolan M. C., Praet A., Rozitis B., Sandford S. A., Schrader D. L., Thomas C. A., Zou X.-D., Lauretta D. S., and Osiris-Rex Team. 2019. Evidence for widespread hydrated minerals on asteroid (101955) Bennu. *Nature Astronomy* 3:332–340.
- Hanna R. D. and Ketcham R. A. 2017. X-ray computed tomography of planetary materials: A primer and review of recent studies. *Chemie der Erde Geochemistry*. 77:547572.
- Hanna R. D. and Ketcham R. A. 2018. Evidence for accretion of fine-grained rims in a turbulent nebula for CM Murchison. *Earth and Planetary Science Letters*. 481:201–211.
- Hanna R. D., Hamilton V. E., Haberle C. W., Kaplan H. H., Howell E. S., Takir D., Zolensky M. E., and Lauretta D. S. 2019. What is the hydrated phase on Bennu's surface?. LPI Contribution 2189. Houston, Texas: Lunar and Planetary Institute.
- Hanna R. D., Hamilton V. E., Haberle C. W., King A. J., Abreu N. M., and Friedrich J. M. 2020. Distinguishing relative aqueous alteration and heating among CM chondrites with IR spectroscopy. *Icarus* 346:113–760.

- Harries D. and Barth M. I. F. 2017. Sulfide, oxide, and nitride formation in CM chondrites: A connection to the formation of type II chondrules involving ices? (abstract #6201). *Meteoritics & Planetary Science* 52.
- Harries D. and Langenhorst F. 2013. The nanoscale mineralogy of Fe, Ni sulfides in pristine and metamorphosed CM and CM/CI-like chondrites: Tapping a petrogenetic record. *Meteoritics & Planetary Science* 48:879–903.
- Horstmann M. and Bischoff A. 2014. The Almahata Sitta polymict breccia and the late accretion of Asteroid 2008 TC<sub>3</sub>—Invited review. *Chemie der Erde—Geochemistry* 74:149–184.
- Jutzi M. and Michel P. 2020. Collisional heating and compaction of small bodies: Constraints for their origin and evolution. *Icarus* 350:113–867.
- Kebukawa Y., Ito M., Zolensky M. E., Greenwood R. C., Rahman Z., Suga H., Nakato A., Chan Q. H., Fries M., and Takeichi Y. 2019. A novel organic-rich meteoritic clast from the outer solar system. *Scientific Reports* 9:3169.
- Kebukawa Y., Zolensky M. E., Mathurin J., Dartois E., Engrand C., Duprat J., Deniset-Besseau A., Dazzi A., Fries M., Ohigashi T., Wakabayashi D., Yamashita S., Takeichi Y., Takahashi Y., Kondo M., Ito M., Kodama Y., Rahman Z., and Kobayashi K. 2020. Organic matter in the Aguas Zarcas (CM2) meteorite: High abundance of aliphatic carbon in metal-rich lithology (abstract #1349). 51st Lunar and Planetary Science Conference. CD-ROM.
- Kerraouch I., Zolensky M. E., Bischoff A., Le L., Belhai D., Patzek M., and Ebert S. 2018. Mineralogical study of a white clast from Murchison (CM2): Comparison with R chondrites (abstract #6363). *Meteoritics & Planetary Science* 53.
- Kerraouch I., Ebert S., Patzek M., Bischoff A., Zolensky M. E., Pack A., Schmitt-Kopplin P., Belhai D., Bendaoud A., and Le L. 2019a. A light, chondritic xenolith in the Murchison (CM) chondrite—Formation by fluid-assisted percolation during metasomatism? *Geochemistry—Chemie der Erde* 79:125518.
- Kerraouch I., Bischoff A., Zolensky M. E., Ebert S., Patzek M., Pack A., Schmitt-Kopplin P., Belhai D., Bendaoud A., and Le L. 2019b. A chondritic xenolith in the Murchison (CM2) chondrite formed by fluid-assisted percolation during metasomatism (abstract). *Meteoritics & Planetary Science* 54:A6197.
- Kerraouch I., Bischoff A., Zolensky M. E., Pack A., Patzek M., Wölfer E., Burkhardt C., and Fries M. 2020. Characteristics of a new carbonaceous, metal-rich lithology found in the carbonaceous chondrite breccia Aguas Zarcas (abstract #2011). 51st Lunar and Planetary Science Conference. CD-ROM.
- King A. J., Schofield P. F., and Russell S. S. 2017. Type I aqueous alteration in CM carbonaceous chondrites: Implications for the evolution of water-rich asteroids. *Meteoritics & Planetary Science* 52:1197–1215.
- Kitazato K., Milliken R. E., Iwata T., Abe M., Ohtake M., Matsuura S., Arai T., Nakauchi Y., Nakamura T., Matsuoka M., Senshu H., Hirata N., Hiroi T., Pilorget C., Brunetto R., Poulet F., Riu L., Bibring J.-P., Takir D., Domingue D. L., Vilas F., Barucci M. A., Perna D., Palomba E., Galiano A., Tsumura K., Osawa T., Komatsu M., Nakato A., Arai T., Takato N., Matsunaga T., Takagi Y., Matsumoto K., Kouyama T., Yokota Y., Tatsumi E., Sakatani N., Yamamoto Y., Okada T., Sugita S., Honda R., Morota T., Kameda S., Sawada H., Honda C., Yamada M., Suzuki H., Yoshioka K., Hayakawa M., Ogawa K., Cho Y., Shirai K., Shimaki Y., Hirata N., Yamaguchi A., Ogawa N., Terui F., Yamaguchi T., Takei Y., Saiki T., Nakazawa S., Tanaka S., Yoshikawa M., Watanabe S., and Tsuda Y. 2019. The surface composition of asteroid 162173 Ryugu from Hayabusa2 near-infrared spectroscopy. *Science* 364:272–275.
- Lauretta D. S. 2005. Sulfidation of an iron–nickel–chromium–cobalt–phosphorus alloy in 1% H<sub>2</sub>S–H<sub>2</sub> gas mixtures at 400–1000 °C. *Oxidation of Metals* 64:1–22.
- Lauretta D. S., Dellagiustina D. N., Bennett C. A., Golish D. R., Becker K. J., Balram-Knutson S. S., Barnouin O. S., Becker T. L., Bottke W. F., Boynton W. V., Campins H., Clark B. E., Connolly H. C., Drouet D’Aubigny C. Y., Dworkin J. P., Emery J. P., Enos H. L., Hamilton V. E., Hergenrother C. W., Howell E. S., Izawa M. R. M., Kaplan H. H., Nolan M. C., Rizk B., Roper H. L., Scheeres D. J., Smith P. H., Walsh K. J., Wolner C. W. V., and the OSIRIS-REx Team. 2019a. The unexpected surface of asteroid (101955) Benu. *Nature* 568:55–60. <https://doi.org/10.1038/s41586-019-1033-6>.
- Lauretta D. S., Hergenrother C. W., Chesley S. R., Leonard J. M., Pelgrift J. Y., Adam C. D., Al Asad M., Antreasian P. G., Ballouz R. L., Becker K. J., Bennett C. A., Bos B. J., Bottke W. F., Brozović M., Campins H., Connolly H. C., Daly M. G., Davis A. B., de León J., DellaGiustina D. N., Drouet d’Aubigny C. Y., Dworkin J. P., Emery J. P., Farnocchia D., Glavin D. P., Golish D. R., Hartzell C. M., Jacobson R. A., Jawin E. R., Jenniskens P., Kidd J. N., Lessac-Chenen E. J., Li J.-Y., Libourel G., Licandro J., Liounis A. J., Maleszewski C. K., Manzoni C., May B., McCarthy L. K., McMahon J. W., Michel P., Molaro J. I., Moreau M. C., Nelson D. S., Owen W. M., Rizk B., Roper H. I., Rozitis B., Sahr E. M., Scheeres D. J., Seabrook J. A., Selznick S. H., Takahashi Y., Thuillet F., Tricarico P., Vokrouhlický D., and Wolner C. W. V. 2019b. Episodes of particle ejection from the surface of the active asteroid (101955) Benu. *Science* 366:6470. <https://doi.org/10.1126/science.aay3544>.
- Lentfort S., Bischoff A., Ebert S., and Patzek M. 2020. Classification of CM chondrite breccias—Implications for the evaluation of samples from the OSIRIS-REx and Hayabusa2 missions. *Meteoritics & Planetary Science*. <https://doi.org/10.1111/MAPS.13486>
- Lindgren P., Lee M. R., Sofe M. R., and Zolensky M. E. 2013. Clasts in the CM2 carbonaceous chondrite Lonewolf Nunataks 94101: Evidence for aqueous alteration prior to complex mixing. *Meteoritics & Planetary Science* 48:1074–1090.
- Mackinnon I. D. and Zolensky M. E. 1984. Proposed structures for poorly characterized phases in C2M carbonaceous chondrite meteorites. *Nature* 309:240–242.
- MacPherson G. J. and Davis A. M. 1994. Refractory inclusions in the prototypical CM chondrite, Mighei. *Geochimica et Cosmochimica Acta* 58:5599–5625.
- Matsuoka M., Nakamura T., Kimura Y., Hiroi T., Nakamura R., Okumura S., and Sasaki S. 2015. Pulse-laser irradiation experiments of Murchison CM2 chondrite for reproducing space weathering on C-type asteroids. *Icarus* 254:135–143.
- McCoy T. J., Connolly H. C., Corrigan C. M., Jawin E. R., Sandford S., Molaro J., DellaGiustina D. N., Rizk B., Nolan M. C., Lauretta D. S., and the OSIRIS-REx Team.



2019. Brecciated boulders: Evidence for impact mixing on Benu's parent body (abstract #6428). *Meteoritics & Planetary Science* 54.
- Metzler K., Bischoff A., and Stöffler D. 1992. Accretionary dust mantles in CM-chondrites: Evidence for nebula processes. *Geochimica et Cosmochimica Acta* 56:2873–2897.
- Michel P., Ballouz R. L., Barnouin O. S., Jutzi M., Walsh K. J., May B. H., Manzoni C., Richardson D. C., Schwartz S. R., Sugita S., Watanabe S., Miyamoto H., Hirabayashi M., Bottke W. F., Connolly H. C., Yoshikawa M., and Lauretta D. S. 2020. Collisional formation of top-shaped asteroids and implications for the origins of Ryugu and Benu. *Nature* 11:2655.
- Morlok A., Bischoff A., Stephan T., Floss C., Zinner E. K., and Jessberger E. K. 2006. Brecciation and chemical heterogeneities of CI chondrites. *Geochimica et Cosmochimica Acta* 70:5371–5394.
- Nakamura T. 2005. Post-hydration thermal metamorphism of carbonaceous chondrites. *Journal of Mineralogical and Petrological Sciences* 100:260–272.
- Pack A., Tanaka R., Hering M., Sengupta S., Peters S., and Nakamura E. 2016. The oxygen isotope composition of San Carlos olivine on VSMOW2-SLAP2 scale. *Rapid Communications in Mass Spectrometry* 30:1495–1504.
- Palmer E. E. and Lauretta D. S. 2011. Aqueous alteration of kamacite in CM chondrites. *Geochimica et Cosmochimica Acta* 75:1587–1607.
- Patzek M., Bischoff A., Visser R., and John T. 2018a. Mineralogy of volatile-rich clasts in brecciated meteorites. *Meteoritics & Planetary Science* 53:2519–2540.
- Patzek M., Pack A., Bischoff A., Visser R., and John T. 2018b. O-isotope composition of CI- and CM-like clasts in ureilites, HEDs, and CR chondrites (abstract #6254). *Meteoritics & Planetary Science* 53.
- Rubin A. E. 2012. Collisional facilitation of aqueous alteration of CM and CV carbonaceous chondrites. *Geochimica et Cosmochimica Acta* 90:181–194.
- Rubin A. E. and Wasson J. T. 1986. Chondrules in the Murray CM2 meteorite and compositional differences between CM-CO and ordinary chondrite chondrules. *Geochimica et Cosmochimica Acta* 50:307–315.
- Rubin A. E., Trigo-Rodríguez J. M., Huber H., and Wasson J. T. 2007. Progressive aqueous alteration of CM carbonaceous chondrites. *Geochimica et Cosmochimica Acta* 71:2361–2382.
- Sharp Z. D. 1990. A laser based microanalytical method for the in situ determination of oxygen isotope ratios of silicates and oxides. *Geochimica et Cosmochimica Acta* 54:1353–1357.
- Singerling S. A. and Brearley A. J. 2020. Altered primary iron sulfides in CM2 and CR2 carbonaceous chondrites: Insights into parent body processes. *Meteoritics & Planetary Science* 55:496–523.
- Sugita S., Honda R., Morota T., Kameda S., Sawada H., Tatsumi E., Yamada M., Honda C., Yokota Y., Kouyama T., Sakatani N., Ogawa K., Suzuki H., Okada T., Namiki N., Tanaka S., Iijima Y., Yoshioka K., Hayakawa M., Cho Y., Matsuoka M., Hirata N., Hirata N., Miyamoto H., Domingue D., Hirabayashi M., Nakamura T., Hiroi T., Michikami T., Michel P., Ballouz R.-L., Barnouin O. S., Ernst C. M., Schröder S. E., Kikuchi H., Hemmi R., Komatsu G., Fukuhara T., Taguchi M., Arai T., Senshu H., Demura H., Ogawa Y., Shimaki Y., Sekiguchi T., Müller T. G., Hagermann A., Mizuno T., Noda H., Matsumoto K., Yamada R., Ishihara Y., Ikeda H., Araki H., Yamamoto K., Abe S., Yoshida F., Higuchi A., Sasaki S., Oshigami S., Tsuruta S., Asari K., Tazawa S., Shizugami M., Kimura J., Otsubo T., Yabuta H., Hasegawa S., Ishiguro M., Tachibana S., Palmer E., Gaskell R., Le Corre L., Jaumann R., Otto K., Schmitz N., Abell P. A., Barucci M. A., Zolensky M. E., Vilas F., Thuillet F., Sugimoto C., Takaki N., Suzuki Y., Kamiyoshihara H., Okada M., Nagata K., Fujimoto M., Yoshikawa M., Yamamoto Y., Shirai K., Noguchi R., Ogawa N., Terui F., Kikuchi S., Yamaguchi T., Oki Y., Takao Y., Takeuchi H., Ono G., Mimasu Y., Yoshikawa K., Takahashi T., Takei Y., Fujii A., Hirose C., Nakazawa S., Hosoda S., Mori O., Shimada T., Soldini S., Iwata T., Abe M., Yano H., Tsukizaki R., Ozaki M., Nishiyama K., Saiki T., Watanabe S., and Tsuda Y. 2019. The geomorphology color and thermal properties of Ryugu: Implications for parent-body processes. *Science* 364:252.
- Tanbakouei S., Trigo-Rodríguez J. M., Blum J., Williams I., and Llorca J. 2020. Comparing the reflectivity of ungrouped carbonaceous chondrites with that of short period comets like 2P/Encke. *Astronomy & Astrophysics* 641:A58–A67.
- The Meteoritical Bulletin Database. <https://www.lpi.usra.edu/meteor/metbull.php>. Accessed November 28, 2019.
- Tomeoka K. and Buseck P. R. 1985. Hydrated interplanetary dust particle linked with carbonaceous chondrites? *Nature* 314:338–340.
- Tonui E., Zolensky M., Hiroi T., Nakamura T., Lipschutz M., Wang M.-S., and Okudaira K. 2014. Petrographic, chemical and spectroscopic evidence for thermal metamorphism in carbonaceous chondrites I: CI and CM chondrites. *Geochimica et Cosmochimica Acta* 126:284–306.
- Trigo-Rodríguez J. M. 2015. Aqueous alteration in chondritic asteroids and comets from the study of carbonaceous chondrites. *Planetary Mineralogy, European Mineralogical Union Notes in Mineralogy* 15:67–87.
- Trigo-Rodríguez J. M. and Blum J. 2009. Tensile strength as an indicator of the degree of primitiveness of undifferentiated bodies. *Planetary and Space Science* 57:243–249.
- Trigo-Rodríguez J. M., Rubin A. E., and Wasson J. T. 2006. Non-nebular origin of dark mantles around chondrules and inclusions in CM chondrites. *Geochimica et Cosmochimica Acta* 70:1271–1290.
- Trigo-Rodríguez J. M., Rimola A., Tanbakouei S., Cabedo-Soto V., and Lee M. 2019. Accretion of water in carbonaceous chondrites: Current evidence and implications for the delivery of water to early Earth. *Space Science Reviews* 215:18–27.
- Trinquier A., Elliott T., Ulfbeck D., Coath C., Krot A. N., and Bizzarro M. 2009. Origin of nucleosynthetic isotope heterogeneity in the solar protoplanetary disk. *Science* 324:374–376.
- Watanabe S., Hirabayashi M., Hirata N., Na H., Noguchi R., Shimaki Y., Ikeda H., Tatsumi E., Yoshikawa M., Kikuchi S., Yabuta H., Nakamura T., Tachibana S., Ishihara Y., Morota T., Kitazato K., Sakatani N., Matsumoto K., Wada K., Senshu H., Honda C., Michikami T., Takeuchi H., Kouyama T., Honda R., Kameda S., Fuse T., Miyamoto H., Komatsu G., Sugita S., Okada T., Namiki N., Arakawa M., Ishiguro M., Abe M., Gaskell R., Palmer E., Barnouin O. S., Michel P.,

- French A. S., McMahon J. W., Scheeres D. J., Abell P. A., Yamamoto Y., Tanaka S., Shirai K., Matsuoka M., Yamada M., Yokota Y., Suzuki H., Yoshioka K., Cho Y., Tanaka S., Nishikawa N., Sugiyama T., Kikuchi H., Hemmi R., Yamaguchi T., Ogawa N., Ono G., Mimasu Y., Yoshikawa K., Takahashi T., Takei Y., Fujii A., Hirose C., Iwata T., Hayakawa M., Hosoda S., Mori O., Sawada H., Shimada T., Soldini S., Yano H., Tsukizaki R., Ozaki M., Iijima Y., Ogawa K., Fujimoto M., Ho T.-M., Moussi A., Jaumann R., Bibring J.-P., Krause C., Terui F., Saiki T., Nakazawa S., and Tsuda Y. 2019. Hayabusa2 arrives at the carbonaceous asteroid 162173 Ryugu—A spinning top-shaped rubble pile. *Science* 364:268–272.
- Weisberg M. K. and Huber H. 2007. The GRO 95577 CR1 chondrite and hydration of the CR parent body. *Meteoritics & Planetary Science* 42:1495–1503.
- Weisberg M. K., Prinz M., Clayton R. N., and Mayeda T. K. 1993. The CR (Renaazo-type) carbonaceous chondrite group and its implications. *Geochimica et Cosmochimica Acta* 57:1567–1586.
- Weisberg M. K., Prinz M., Clayton R. N., Mayeda T. K., Grady M. M., and Pillinger C. T. 1995. The CR chondrite clan. *Proceedings of the NIPR Symposium on Antarctic Meteorites* 8:11–32.
- Zhang J., Dauphas N., Davis A. M., Leya I., and Fedkin A. 2012. The proto-Earth as a significant source of lunar material. *Nature Geoscience* 5:251–255.
- Zolensky M. E. and Ivanov A. 2003. The Kaidun microbreccia meteorite: A harvest from the inner and outer asteroid belt. *Chemie der Erde—Geochemistry* 63:185–246.
- Zolensky M. E. and McSween H. Y. Jr. 1988. Aqueous alteration. In *Meteorites and the early solar system*, edited by Kerridge J. F. and Matthews M. S. Tucson, Arizona: The University of Arizona Press. pp. 114–143.
- Zolensky M. E., Barrett R. A., and Browning L. 1993. Mineralogy and composition of matrix and chondrule rims in carbonaceous chondrites. *Geochimica et Cosmochimica Acta* 57:3123–3148.
- Zolensky M. E., Weisberg M. K., Buchanan P. C., and Mittlefehldt D. W. 1996. Mineralogy of carbonaceous chondrite clasts in HED achondrites and the Moon. *Meteoritics & Planetary Science* 31:518–537.
- Zolensky M. E., Mittlefehldt D. W., Lipschutz M. E., Wang M.-S., Clayton R. N., Mayeda T., Grady M. M., Pillinger C., and Barber D. 1997. CM chondrites exhibit the complete petrologic range from type 2 to 1. *Geochimica et Cosmochimica Acta* 61:5099–5115.
- Zolensky M. E., Gregory T., Takenouchi A., Nishiizumi K., Trieman A., Berger E., Le L., Fagan A., Velbel M., Imae N., Yamaguchi A., and Caffee M. 2015. CM carbonaceous chondrite lithologies and their space exposure ages. 2015 NIPR Symposium on Antarctic Meteorites.
- Zolensky M., Takenouchi A., Gregory T., Nishiizumi K., Caffee M., Velbel M., Ross K., Zolensky A., Le L., and Imae N. 2017. The relationship between cosmic-ray exposure ages and mixing of CM chondrite lithologies (abstract #2094). 48th Lunar and Planetary Science Conference. CD-ROM.

## SUPPORTING INFORMATION

Additional supporting information may be found in the online version of this article.

**Figure S1.** XCT images of JSC-40 (a, b) and UTA-2 (c) samples.

**Table S1.** Fragments of Aguas Zarcas used in this study with their characteristics and methods applied.